Aircraft Regional-Scale Flux Measurements over Complex Landscapes of Mangroves, Desert, and Marine Ecosystems of Magdalena Bay, Mexico

Aircraft Regional-Scale Flux Measurements over Complex Landscapes of Mangroves, Desert, and Marine Ecosystems of Magdalena Bay, Mexico

ROMMEL C. ZULUETA,* WALTER C. OECHEL, JOSEPH G. VERFAILLIE,+ AND STEVEN J. HASTINGS

Global Change Research Group, Department of Biology, San Diego State University, San Diego, California

BENIAMINO GIOLI

IBIMET-CNR, Firenze, Italy

WILLIAM T. LAWRENCE

Natural Sciences Department, Bowie State University, Bowie, Maryland

KYAW THA PAW U

Department of Land, Air, and Water Resources, University of California, Davis, Davis, California

(Manuscript received 2 February 2012, in final form 21 February 2013)

ABSTRACT

Natural ecosystems are rarely structurally simple or functionally homogeneous. This is true for the complex coastal region of Magdalena Bay, Baja California Sur, Mexico, where the spatial variability in ecosystem fluxes from the Pacific coastal ocean, eutrophic lagoon, mangroves, and desert were studied. The Sky Arrow 650TCN environmental research aircraft proved to be an effective tool in characterizing land–atmosphere fluxes of energy, CO_2, and water vapor across a heterogeneous landscape at the scale of 1 km. The aircraft was capable of discriminating fluxes from all ecosystem types, as well as between nearshore and coastal areas a few kilometers distant. Aircraft-derived average midday CO_2 fluxes from the desert showed a slight uptake of $-1.32\,\mu\text{mol}\,CO_2\,m^{-2}\,s^{-1}$, the coastal ocean also showed an uptake of $-3.48\,\mu\text{mol}\,CO_2\,m^{-2}\,s^{-1}$, and the lagoon mangroves showed the highest uptake of $-8.11\,\mu\text{mol}\,CO_2\,m^{-2}\,s^{-1}$. Additional simultaneous measurements of the normalized difference vegetation index (NDVI) allowed simple linear modeling of CO_2 flux as a function of NDVI for the mangroves of the Magdalena Bay region. Aircraft approaches can, therefore, be instrumental in determining regional CO_2 fluxes and can be pivotal in calculating and verifying ecosystem carbon sequestration regionally when coupled with satellite-derived products and ecosystem models.

1. Introduction

A ubiquitous problem in carbon cycle science is one of adequate sampling, both in time and in space, to infer processes and annual budgets. This problem is typified by the difficulty in determining representative plot and tower measurements that can be extrapolated to larger landscapes and regions (Desai et al. 2008). Understanding the processes and controls in carbon flux enough to make predictions because of climate change are often done at the ecosystem level (micrometeorological studies), while regional-to-global feedbacks, under both current and future conditions, are often done at larger regional scales embodying synoptic-scale weather patterns (Turner et al. 2004).

Models and satellite-based remote sensing observations are often used to estimate fluxes of mass and energy at larger spatial scales. However, empirical data to verify these models and satellite-derived products,

* Current affiliation: National Ecological Observatory Network, Inc., Boulder, Colorado.

+ Current affiliation: Department of Environmental Science, Policy and Management, University of California, Berkeley, Berkeley, California.

Corresponding author address: Rommel C. Zulueta, National Ecological Observatory Network, Inc., 1685 38th St., Suite 100, Boulder, CO 80301.
E-mail: rzulueta@neoninc.org

DOI: 10.1175/JTECH-D-12-00022.1

which establish mechanistic linkages among scales of measurement, are often lacking (Desai et al. 2008). Ecosystem flux estimates scaled from a single tower-based measurement to the landscape or regional scale typically lack sufficient spatial density to adequately represent the region's heterogeneity in structure and process (see, e.g., Zulueta et al. 2011). Even ecosystems considered homogeneous (e.g., grasslands and tundra) can have a large degree of functional variability over short distances (from meters to kilometers), making the assimilation of plot level and tower measurements with regional and global estimates challenging (Desai et al. 2010). The key to understanding the regional patterns and controls on mass and energy fluxes in terrestrial and aquatic ecosystems is the development of new methodologies that link and constrain the multiple scales of interest (Dolman et al. 2009).

Typically, when assessing carbon flux in terrestrial ecosystems, predominant ecosystem types are selected and monitored because they are assumed to be representative of the regional flux. However, multiple factors cause spatial variability in the surface fluxes. These include variations in edaphic factors, topography, hydrology, vegetation composition and function, land use, disturbance history, and so on. These variations are often not measured or monitored, and their relative importance is often not fully understood or explored. This is particularly true in areas where ecosystems are remote, such as the Arctic and tropics, or logistically difficult to adequately measure, such as complex coastal ecosystems.

Assessing the spatial variability in surface fluxes in complex ecosystems is important to understanding the role they play in local and regional carbon balance; specifically in systems that provide important ecosystem services and have high economic value (e.g., the subtropical mangrove forests along the Baja California, Mexico, coastline). One such system is the mangrove forests along Magdalena Bay, the largest expanse of mangrove forests along the Pacific coast of Baja California, Mexico. Magdalena Bay and the surrounding mangrove areas and coastal estuaries sustain a variety of resident and migratory waterfowl (see Zarate-Ovando et al. 2006), are a feeding and developmental area for five of the world's seven sea turtle species (see Cliffton et al. 1995), are one of the major winter breeding lagoons for the North Pacific gray whale *Eschrichtius robustus* (see Urban et al. 2003), and are also a key regional fishing and recreational area. Magdalena Bay has an extensive lagoon area with mangrove forests surrounded by barrier islands and the Pacific Ocean to the west, a central lagoon, and desert eastward of the lagoon to the landward side.

Mangrove forests and subtropical coastal ecosystems are disappearing at a rapid rate. Over the past two decades, over 35% of the world's mangrove forests have been lost and converted to other land use (Valiela et al. 2001). Despite the mangroves' high economic value, ecosystem services (Costanza et al. 1997; Nagelkerken et al. 2008; Reid et al. 2006), and role in global carbon cycling (Bouillon et al. 2008), they continue to be severely disrupted by tourism developments, exploitation, and aquaculture (Alongi 2002; Duke et al. 2007; Valiela et al. 2001). In May 2004, the Mexican government repealed a law protecting mangroves, which opened the way for extensive coastal developments exacerbating the severe pressure from land use, development, and shrimp farming (Glenn et al. 2006; Paez-Osuna et al. 2003). Though a new mangrove protection law was passed in February 2007, growth and interest in nautical and ecotourism in Mexico continue to rise. Plans are currently underway to expand and modernize 13 existing marinas and construct 11 new commercial ports and coastal resorts along the coast of Baja California and the Sea of Cortez (e.g., the Escalera Nautica project). Continued exploitation and development along these coastlines could threaten previously undeveloped, unprotected mangrove forests and coastal estuaries including those within Magdalena Bay.

The Magdalena Bay area provides a case study for these mangrove forests and also allows comparisons of the ecosystem functioning of vastly different ecosystems with the same synoptic-scale climate patterns, and contrasting microclimate, over relatively short distances. In this study, we use an aircraft-based eddy covariance system to examine the spatial variability in fluxes across various landscapes for the complex Pacific coastal ecosystem in northern Magdalena Bay, Baja California Sur (BCS), Mexico. Since direct measurements and regional estimates of mangrove forest net productivity are limited in this area, an overall goal of this research was to estimate the midday net ecosystem CO_2 flux of the mangrove forest area of the Magdalena Bay region with aircraft and satellite measurements. The questions we address are (i) do aircraft-based flux measurements have sufficient sampling resolution to detect differences in process rates among adjacent coastal ecosystems (desert, mangrove, lagoon, and ocean) only a few kilometers apart, and (ii) how do the magnitude and direction of the fluxes differ among the several ecosystems of the area?

2. Materials and methods

a. Site description

These data presented here were collected between 24 and 28 July 2004, in the vicinity of Puerto Aldofo Lopez Mateos (25.192 450°N, 112.115 783°W; hereafter referred

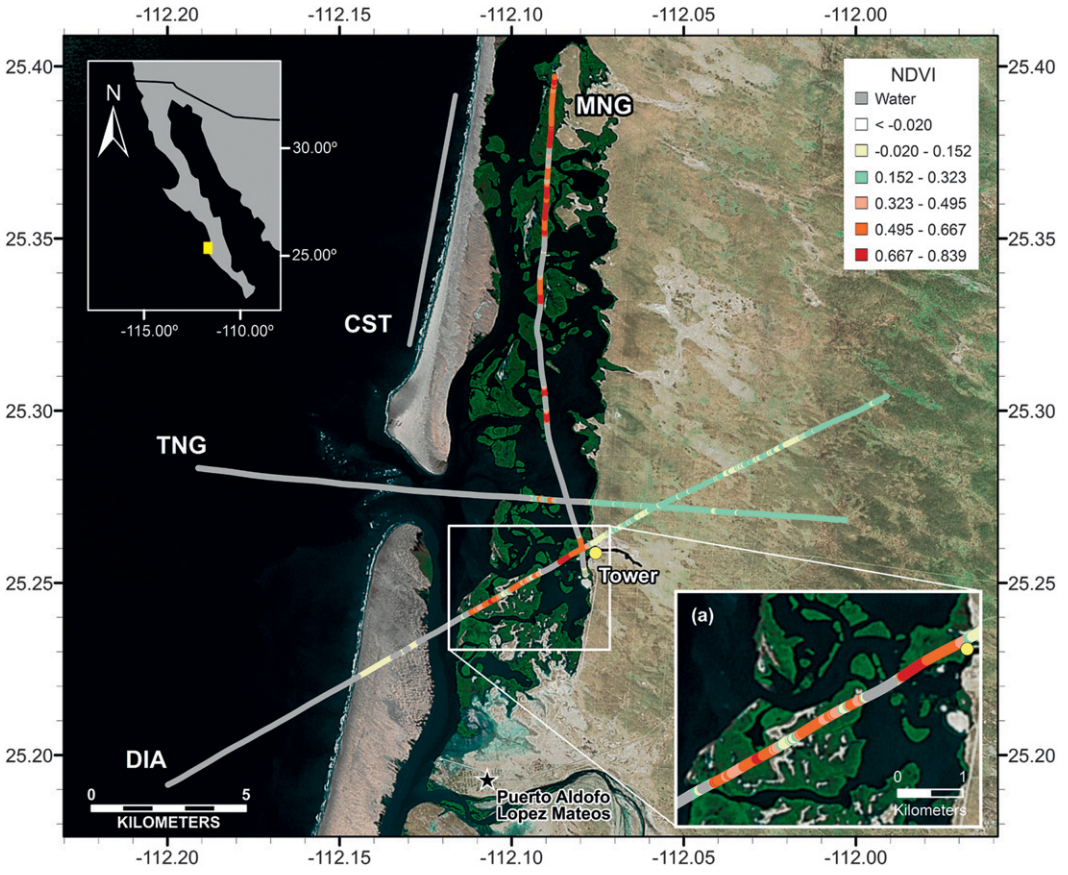

FIG. 1. Lopez Mateos in the northern region of Magdalena Bay. The four flight transects are identified as DIA, TNG, CST, and MNG (see Table 3 for transect details). Transect NDVI is derived from the onboard hyperspectral instrument with an effective pixel size of 1.78 m × 5.06 m. (a) Emphasis of the ability to resolve fine surface details with the onboard hyperspectral instrumentation. The closest approach of the aircraft to the portable EC tower along the DIA and MNG transects were 10- and 20-m horizontal separation, respectively. Base imagery is courtesy of TerraMetrics.

to as Lopez Mateos; Fig. 1). This is a small fishing town located in BCS, Mexico, along the northern extent of the Magdalena Bay lagoon. This northern area is protected from the Pacific Ocean by the Isla Magdalena, a sandy barrier island that parallels the mainland coastline and has three distinct canals to the ocean. The closest canal is the Boca la Soledad, which is 9 km to the northwest of the town.

The area is in a subdivision of the Sonoran Desert classified as the Magdalena region (Shreve and Wiggins 1964); the regional terrestrial vegetation is sparse and generally described as desert scrub (Turner and Brown 1982; Wiggins 1980). The precipitation regime in the Magdalena region is seasonally variable with an annual precipitation of 125 mm, with the majority of the precipitation occurring in the fall and winter (89 mm) with the summer and spring having the lowest amounts, 31 and 5 mm, respectively (Hastings and Turner 1965).

The desert surrounding Lopez Mateos is generally sand with scattered rocky outcroppings. The larger dominant plant species are drought and salt tolerant and include cacti such as *Stenocereus thurberi*, *Opuntia cholla*, and numerous large individuals (>5 m tall) of the columnar cactus *Pachycereus pringlei* and some trees such as *Bursera microphylla*, *Bursera hindsiana*, *Simondsia chinensis*, and *Larrea tridentata*. *Ambrosia magdalanae* is a common herbaceous plant. The coastal margins adjacent to the desert and mangrove lagoon include perennial species of *Isocoma menziesii*, *Monanthochloe littoralis*, and *Suaeda monquinii*, while the salt marshes along the lagoon edges are occupied by halophytes including *Allenrolfea occidentalis*, *Batis maritime*, *Salicornia bigelovii*, and *Sesuvium portulacastrum*. The sand dunes have sparse coverage of *Abronia maritima* and *Lotus bryantii*. Although it is part of the Sonoran Desert, the Magdalena region contains endemic and expansive

TABLE 1. Footprint estimations for each ecosystem type along the aircraft flight transects with the footprint estimation of the portable tower included for comparison. Each flight transect is separated based on their respective desert, mangrove, and ocean sections and combined together to get the average footprint estimations. The measurement height is z, u_* is the friction velocity, ws is average horizontal wind speed, σ_w is the standard deviation of the vertical wind, z_0 is the roughness length, x_{max} is the peak contribution distance of the footprint function, and $x_{90\%}$ is the upwind distance from the measurement location where 90% of the flux contribution is included within the footprint.

Section	z (m)	u_* (m s^{-1})	ws (m s^{-1})	σ_w (m s^{-1})	z_0 (m)	x_{max} (m)	$x_{90\%}$ (m)
Desert	10.47 ± 1.66	0.51 ± 0.13	5.35 ± 1.49	0.59 ± 0.09	0.68 ± 0.36	94.79 ± 23.42	259.63 ± 64.15
Mangrove	8.05 ± 1.22	0.46 ± 0.15	5.14 ± 1.36	0.52 ± 0.12	0.54 ± 0.32	79.26 ± 17.12	217.11 ± 46.91
Ocean	7.54 ± 1.22	0.26 ± 0.06	6.71 ± 1.19	0.25 ± 0.04	0.15 ± 0.1	110.7 ± 21.74	303.23 ± 59.54
Mangrove (near portable tower)	7.98 ± 0.89	0.47 ± 0.1	5.07 ± 1.26	0.52 ± 0.1	0.52 ± 0.2	78.22 ± 14.63	214.27 ± 40.07
Portable tower	4.2	0.44 ± 0.17	2.17 ± 0.89	0.52 ± 0.18	0.57 ± 0.12	38.09 ± 1.6	104.34 ± 4.39

mangrove lagoons in protected coves of Magdalena Bay on the western coast.

Magdalena Bay is a subtropical lagoon system with mangrove forests lining the inside interior coastline of the protected bay and natural shallow channels (Alvarez-Borrego et al. 1975). This eutrophic coastal lagoon has higher salinity than the open ocean because of its low annual precipitation, high rate of evaporation, and minimal freshwater inputs from the land (Alvarez-Borrego et al. 1975). The dominant mangrove species are the red (*Rhizophora mangle*), white (*Laguncularia racemosa*), and, to a lesser extent, black (*Avicennia germinans*) mangrove trees. The Magdalena Bay region spans between 25.73° and 24.27°N and 111.32° and 112.35°W and covers an area of approximately 1409 km^2 of which the mangrove forest is estimated to cover 361.23 km^2 (determined in this study). The average tree height and stem diameter were 3.15 m and 4.09 cm, respectively, with tree densities within the mangroves estimated at 2569 trees ha^{-1}, with a basal area of 3.21 m^2 ha^{-1} (Chavez 2006).

Detailed descriptions of the Magdalena Bay and surrounding environments can be found in Alvarez-Borrego et al. (1975) with additional information on the physical and biological characteristics of the bay region summarized in Bizzarro (2008).

b. Meteorological conditions during flux flights

All flux flights were conducted under visual flight rules (VFR) conditions from 0930 to 1830 mountain standard time (MST). Clear skies prevailed throughout the campaign with an average photosynthetically active radiation (PAR) of 1365 μmol m^{-2} s^{-1} and reached a maximum of 2224 μmol m^{-2} s^{-1} at about 1300 MST. The average air temperatures varied across the different ecosystems with the average across all the flight transects at 24.3°C with the highest average temperatures observed over the desert (26.8°C) and the lowest over the ocean (22.6°C) with the mangroves at a temperature in between (24.3°C). The highest recorded temperature was at midday over the desert and was 31.7°C.

The wind direction was typically onshore, west–east flow during the day with stable atmospheric conditions occurring at night and early morning. The average wind direction was 282° ± 18.6° with an average speed of 5.7 m s^{-1} across all transects. The horizontal wind speeds varied across the different ecosystems with the highest average speeds over the ocean (6.7 m s^{-1}) relating to having the lowest friction velocity u_* and surface roughness z_0, 0.26 m s^{-1} and 0.15 m, respectively. The u_* and z_0 were similar between the desert and mangrove ecosystems, though the desert had the highest values. Additional turbulence parameters during the flux flights are shown in Table 1.

c. San Diego State University Sky Arrow 650TCN environmental research aircraft

The San Diego State University (SDSU) Sky Arrow 650TCN environmental research aircraft (ERA, hereafter referred to as Sky Arrow; Fig. 2) was used to measure fluxes of CO_2, latent (λE) and sensible (H) heat, and momentum. This custom-designed aircraft platform is ideal for atmospheric turbulence measurements because of its narrow stream wise profile, high wing design, slow flight speed, and aft-mounted engine enabling it to fly in the upper surface layer and lower convective boundary layer. The SDSU Sky Arrow (registration number N272SA, serial number cn002) was the first of its kind and received type certification by the U.S. Federal Aviation Administration (FAA) in July 1999. It is an all-composite aircraft with custom-designed mounting ports in the floor of the fuselage and mounting hard points for instrumentation in the nose and horizontal stabilizer (see Fig. 2). Further details and specifications of the SDSU Sky Arrow are listed in Table 2.

The slim airframe and aircraft configuration allows for an unobstructed nose, and the placement of the turbulence sensors within the mean streamline, with minimal distortion from the airframe (Wyngaard 1988), propeller (Kalogiros and Wang 2002b), and up- and sidewash generated by the wings (Crawford et al. 1996a; Garman

FIG. 2. Photograph of the SDSU Sky Arrow 650TCN ERA while parked at the Lopez Mateos airstrip. Locations of the sensors are shown. The BAT probe (inset) is on the nose of the aircraft while the four TANS Vector attitude GPS antennas are located on the center of each wing, top of the engine cowling, and top of the horizontal stabilizer. The data acquisition system and computers are located behind the rear seat. Downward-looking sensors are located in the two view ports in the bottom of the fuselage of the aircraft.

et al. 2008; Kalogiros and Wang 2002b). This aircraft incorporated instrumentation for eddy covariance measurements and low-level remote sensing (Dumas et al. 2001). We used the National Oceanic and Atmospheric Administration (NOAA) Air Resources Laboratory–developed mobile flux platform (MFP) for eddy covariance measurements (Crawford et al. 1990; Hall et al. 2006), which incorporates a nose-mounted Best Air Turbulence (BAT) probe and pressure sphere (Crawford and Dobosy 1992; Hacker and Crawford 1999). A fast-response open-path infrared gas analyzer (IRGA; LI-7500, LI-COR Inc., Lincoln, Nebraska) also located on the nose provided simultaneous measurements of CO_2 and water vapor, and density corrections were applied because of the mass transfer of heat and water vapor from one averaging period to the next (Webb et al. 1980). Dewpoint temperature was measured with a dewpoint hygrometer (DewTrak 200, EdgeTech, Marlborough, Massachusetts) from the underside of the aircraft.

The aircraft attitude was measured using nose and airframe-mounted accelerometers (ICS3022, Measurement Specialties, Hampton, California) and a vector attitude global positioning system (GPS), the Trimble Advanced Navigation System (TANS Vector, Trimble Navigation Ltd., Sunnyvale, California) at 50 and 10 Hz respectively. Blending of the two signals achieved an attitude-sampling frequency of 50 Hz (Eckman et al. 1999) with a $\pm 0.05°$ accuracy. Aircraft position was measured at 10 Hz with a 12-channel L1 frequency GPS (Model 3151, NovAtel Inc., Calgary, Alberta, Canada), which was differentially corrected in postprocessing (Waypoint GrafNav, NovAtel Inc.) with position data from a stationary GPS base station of the same type as on the aircraft.

Simultaneous measurements of incoming and reflected radiation were also measured. Up- and downwelling PAR were made with two silicon quantum sensors (LI-190SB, LI-COR, Inc.) and net radiation was measured with a Fritschen-type net radiometer (Q*7.1, REBS Inc., Seattle, Washington). The net radiometer was not actively aspirated because once in flight the airflow around the sensor met or exceeded its requirements for aspiration. The PAR and net radiation sensors were located on the port side of the aircraft's horizontal stabilizer (see Fig. 2).

Low-level remotely sensed surface temperature was measured with an infrared temperature sensor (4000.4GH, Everest Interscience, Tucson, Arizona), while a laser altimeter was used to measure aircraft altitude above ground level (LD90-3300HR, Riegl, Horn, Austria). Hyperspectral

TABLE 2. Details and specifications for the SDSU Sky Arrow 650TCN ERA.

Aircraft specifications	
Power plant	
Manufacturer	Bombardier Rotax
Model	912F
Power output	59.6 kW at 5800 rpm
Propeller	
Manufacturer	Hoffman
Description	2-blade fixed pitch
Dimensions	
Length	8.15 m*
Height	2.67 m
Wing span	9.68 m
Weights	
Empty weight	460 kg
Maximum takeoff weight	650 kg
Usable load	190 kg
Capacities	
Usable fuel	67.5 L
Endurance	4.25 h
Performance	
Cruise speed	45 m s^{-1}
Stall speed	21 m s^{-1}
Ceiling	4115 m
Takeoff distance	240 m
Landing distance	135 m

* With BAT probe attached, 7.60 m without.

reflectance measurements from 304 to 1134 nm (255 bands, 3.2-nm bins) were made using a dual channel spectrometer (UniSpec-DC, PPSystems, Amesbury, Massachusetts) with a upward facing cosine incident light receptor and a 10° field-of-view downward-looking lens resulting in an average sampling footprint diameter of 1.48 m at the 8.48-m average flight height above the ground. Detector integration times varied with light intensity and ranged from 9 to 20 ms resulting in sampling frequencies from 5 to 10 Hz. Ten integration periods were internally averaged before file storage to the data acquisition system. The average ground speed of the aircraft was 38.2 m s^{-1} so each stored measurement was therefore integrated over an average length of 5.06 m resulting in an effective ''pixel'' resolution of 1.48 m × 5.06 m. A fluoropolymer-based solid thermoplastic calibration panel (Spectralon SRT-99, Labsphere, Sutton, New Hampshire) was measured before and after each flight to correct for variations in solar radiation. The spectral reflectance were interpolated into 1-nm bands and the normalized difference vegetation index (NDVI; Tucker 1979) was calculated using the red (620–670 nm) and near infrared (841–876 nm) wavelengths, which correspond to the *Terra* satellite Moderate Resolution Imaging Spectroradiometer (MODIS) bands 1 (b_1) and 2 (b_2), respectively, and is calculated as

$$\mathrm{NDVI} = \frac{(b_2 - b_1)}{(b_2 + b_1)}. \quad (1)$$

Atmospheric turbulence and wind velocity relative to the aircraft were measured with the nose-mounted BAT probe housing a 9-hole pressure sphere used to measure static pressure and to convert microscale pressure fields into known velocities of the three-dimensional (u, v, and w) winds and their high-frequency fluctuations (Brown et al. 1983; Crawford and Dobosy 1992; Garman et al. 2006; Hacker and Crawford 1999). The fast response temperature fluctuations were measured within the nose hemisphere with a 0.13-mm-diameter microbead thermistor (VECO 32A402A, YSI Inc., Yellow Springs, Ohio) at the hemisphere's stagnation point (Tp_1) and a secondary microbead thermistor located within a ''fast flow'' port at the sphere edge (Tp_2), while the mean air temperature was measured with a Thermilinear network (44212, YSI Inc.) (Crawford and Dobosy 1992).

Calibration of the aircraft's wind vector system was conducted on 28 July 2004 in the morning between 0730 and 0900 MST, over the ocean, at elevations from 1250 to 1575 m above sea level (ASL). Conditions during this time were ideal for a calibration flight as the boundary layer was relatively low to the ground and the mixing layer was not deep (i.e., approximately 340 m ASL) with winds aloft being smooth and consistent. In-flight calibrations of the wind vector system were necessary for the instrument installation positions, aircraft flight performance, and aerodynamics of the aircraft. These calibrations are used to estimate flow distortion, calculate corrections for wind measurements, and ensure synchronization of the data acquisition and measurement instrumentation (Bögel and Baumann 1991; Lenschow 1986; Scott et al. 1990; Vellinga et al. 2013). Modified calibration maneuvers included a constant altitude wind box, standard rate turns (3° s^{-1}), pilot-induced pitch and yaw oscillations, sideslip, and acceleration/deceleration maneuvers (Bögel and Baumann 1991; Kalogiros and Wang 2002a; Khelif et al. 1999; Leise and Masters 1993; Lenschow 1986; Lenschow et al. 2007; Telford et al. 1977; Tjernström and Friehe 1991; Vellinga et al. 2013; Williams and Marcotte 2000). A detailed description of calibration procedures for a similarly instrumented and configured Sky Arrow ERA is presented in Vellinga et al. (2013).

A factory calibration of the IRGA was used at the beginning of the measurement campaign, a field calibration was done on 27 July 2004, and a field calibration was done at the end of the campaign following AmeriFlux protocols (http://public.ornl.gov/ameriflux/sop.shtml). A CO_2-free ultrazero air was used as the zero set point for both the CO_2 and water vapor, NIST-traceable

primary gas standards were used to span the CO_2, and a portable dewpoint generator (LI-610, LI-COR, Inc.) was used to span the water vapor. Following the field calibration, the IRGA was allowed to equilibrate with the ambient environmental conditions with several passes over the flight transects throughout the remainder of the day while other meteorological measurements were made.

The SDSU Sky Arrow ERA infrastructure is further described in Dumas et al. (2001) with additional details described in Zulueta et al. (2011). Two ''sister'' aircraft [one used in the Regional Assessment and Modelling of the Carbon Balance of Europe (RECAB) research project and one operated by the University of Alabama], which have the same airframe but with slightly modified and updated MFP instrumentation packages, are also described in Gioli et al. (2006) and Hall et al. (2006), respectively.

d. Aircraft calculations

The high sampling frequency from the aircraft's instrumentation package allows for computation of fluxes of mass, momentum, and energy using the eddy covariance (EC) technique (Baldocchi et al. 1988; Loescher et al. 2006a,b; Swinbank 1951). This direct measure of surface fluxes is expressed accordingly:

$$F_\phi = \rho\overline{w'\phi'} = \rho\overline{(w-\overline{w})(\phi-\overline{\phi})}, \tag{2}$$

where F is the turbulent scalar flux, ϕ is the flux scalar of interest, ρ is the mean dry air density, w represents the vertical wind fluctuation, primes denote turbulent fluctuations, and overbars denote ensemble averages (aircraft fluxes embody both temporal and spatial averaging).

Eddy covariance measurements from moving platforms such as aircraft are similar to that of stationary ground-based towers with the exception of the adiabatic heating correction for temperature and the measurement of the wind vectors themselves (Leise and Masters 1993; Lenschow 1986). Aircraft carry the wind measurement sensors through turbulent structures within the atmosphere. Because of the angle of attack and continuous motion (pitch, roll, and yaw) of an aircraft while in flight, measurements of the velocity of the instruments V_p must be subtracted from the relative wind velocity V_a in order to determine the winds relative to Earth's surface V:

$$V = V_a - V_p. \tag{3}$$

The velocity V_a was computed from pressure differences observed from the nose hemisphere (Brown et al. 1983; Crawford and Dobosy 1992; Eckman 2012) while V_p is obtained from a blending of both high-frequency accelerometers and low-frequency TANS Vector GPS signals (Eckman et al. 1999). The calculation of these winds was performed in postprocessing using a NOAA-designed C program called makepod, which incorporates the algorithms and techniques described in Leise and Masters (1993), Crawford and Dobosy (1992), Eckman (2012), and Eckman et al. (1999). Calculated wind vectors were then converted and saved to the network Common Data Form (NetCDF) format (Rew et al. 1997).

Tower-based EC calculations typically use an ensemble or temporal average (Baldocchi et al. 1988); however, since aircraft move through the turbulent eddies, changes in aircraft speed must also be considered. Aircraft speed and vertical wind velocity are correlated and can lead to biases if only the temporal covariances are used (Crawford et al. 1993a). Wind updrafts result in aircraft acceleration as the pilot must decrease the angle of attack to maintain constant altitude, resulting in fewer data samples, while wind downdrafts result in a deceleration as the pilot must increase the angle of attack to maintain constant altitude, resulting in more data sampled. Aircraft-based EC calculations therefore require a spatial averaging technique for all variables used in the EC calculations as described in Crawford et al. (1993a) and are defined as

$$[\phi] = \frac{1}{\bar{S}T}\sum_i \phi_i S_i \Delta t, \tag{4}$$

where square brackets indicate the spatial average, ϕ represents the variables in the covariance calculations, S is the aircraft speed, subscript i indicates instantaneous values, Δt is the time increment between measurements, and overbars represent the average over the time T of the calculation segment.

Along with aircraft speed, the measurement height is also a determining factor in the length of the spatial average used for the EC computations. Turbulent eddies increase in size from the surface and longer lengths are therefore required to adequately capture all flux-carrying frequencies (wavelengths). A spatial averaging length would ideally be long enough for adequate turbulence sampling and short enough to differentiate the surface spatial heterogeneity (LeMone et al. 2003). An ogive technique (Desjardins et al. 1989; Friehe et al. 1991; Oncley et al. 1996) can be used to determine the minimum time or length required to capture all flux-carrying frequencies and therefore an optimal spatial averaging length for the aircraft measurements. Determination of the optimal spatial average is done using an ogive function of the integrated cospectrum of the vertical wind velocity and the scalar of interest $Co_{w\phi}$ (Desjardins et al. 1989; Oncley et al. 1996) as

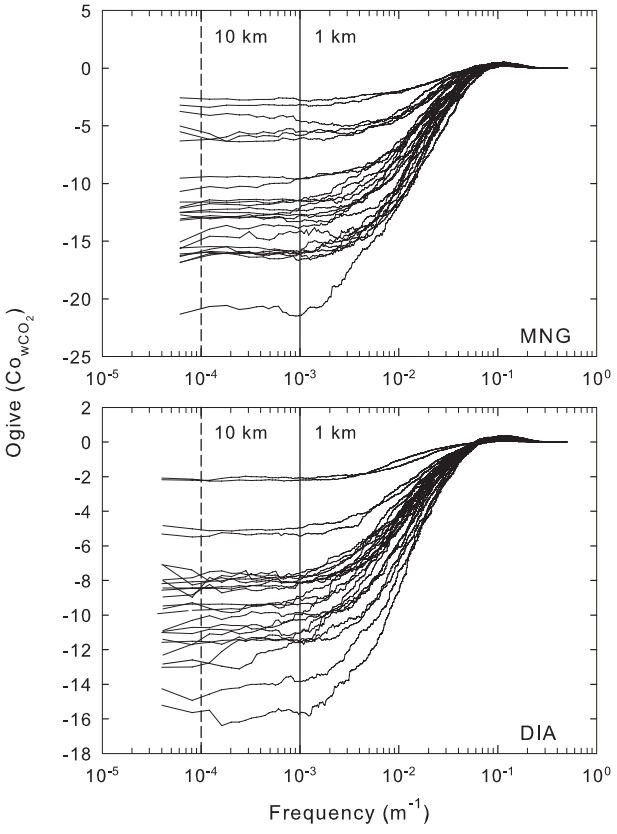

FIG. 3. Ogive plots for all the flux flights (0930–1830 MST) over the MNG and DIA transects (see Fig. 1). The solid vertical line at 1 km shows that a spatial average of 1 km is appropriate to capture nearly all turbulent scales for the flux calculations. The dashed line is at the 10-km spatial scale, and the end of the graph is the total length of each transect.

$$\mathrm{Og}_{w\phi}(f_0) = \int_{\infty}^{f_0} \mathrm{Co}_{w\phi}(f)\, df. \tag{5}$$

High-pass filtering or detrending is not done in order to include all measured fluctuations. The ogive is a cumulative covariance graph over all sampled frequencies up to the full length of the flight transect and shows the cumulative contribution of eddies of increasing size to the total flux. Computations are done over entire data windows from the shortest (a few meters) to the longest (entire transect lengths). The cumulative total is equal to the covariance over the sampling time, and ogive curves that approach an asymptote at the low frequencies suggest that all flux-carrying turbulent scales are constrained within the sampling distance. The optimal averaging length is derived from the frequency at which the ogive curve approaches a constant value (Fig. 3).

The airflow past the microbead thermistor at the nose probe's stagnation point Tp_1 is aspirated at $5\,\mathrm{m\,s^{-1}}$ (Crawford and Dobosy 1992; Hacker and Crawford 1999), while Tp_2 within the fast flow port is subject to the full airspeed (average of $37.0\,\mathrm{m\,s^{-1}}$) of the aircraft while in flight. Initial spectral analysis of the Tp_1 and Tp_2 temperature signals highlighted larger high-frequency signal attenuation for Tp_1, probably related to the reduced airflow over the microbead thermistor at the stagnation point. The Tp_2 microbead thermistor was therefore used for calculations of H (see the appendix). Corrections for the dynamic heating of the temperature probes were applied (Crawford and Dobosy 1992). Adjustments to H to account for the assumed thermodynamic expansion of air from evaporative processes consistent with the assumptions used in the Webb et al. (1980) derivation (Paw U et al. 2000) were also applied.

Resolving the frequencies carrying the largest amount of flux is often limited by the inadequate dynamic response time of the EC sensors, resulting in an attenuation of the measured covariances (Horst 1997; Massman 2000; Moore 1986). This high-frequency attenuation results in some flux loss and can be corrected by calculating transfer functions based on atmospheric stability and theoretical cospectra (Horst 1997, 2000; Massman 2000, 2001; Moore 1986). The flat terrain neutral cospectra described in Kaimal and Finnigan (1994) with data from the 1968 Air Force Cambridge Research Laboratories (AFCRL) Kansas experiments (Kaimal et al. 1972) were used as the theoretical cospectra. To estimate the high-frequency attenuation of first-order instruments with a characteristic time constant τ_c, we used the simplified formula described in Horst (1997):

$$\frac{\langle w'\phi'\rangle_m}{\langle w'\phi'\rangle} = \frac{1}{1 + (2\pi n_m \tau_c \overline{u}/z)^{\alpha}}, \tag{6}$$

where for $z/L \le 0$, $\alpha = 7/8$, and $n_m = 0.085$ and for $z/L > 0$, $\alpha = 1$, and $n_m = 2.0 - 1.915/(1 + 0.5z/L)$. Here, $\langle w'\phi'\rangle_m$ is the measured covariance between the scalar ϕ and w, $\langle w'\phi'\rangle$ is the expected covariance, z denotes the aircraft flight height above the surface (average height 8.48 m), L is the Obukhov length (Foken 2006; Monin and Obukhov 1954; Obukhov 1946, 1971), and $\overline{u}$ is the mean airspeed (average $37.0\,\mathrm{m\,s^{-1}}$). The determined τ_c for Tp_2 was 0.025 s (see the appendix) with overall spectral corrections in the range of 6.2%–12% of the raw fluxes, while the IRGA τ_c was 0.008 s with overall spectral corrections in the range of 4.5%–6.3% of the raw fluxes.

The aircraft-based fluxes were calculated using the 1-km spatial averaging block (approximately 26-s average transit time) determined with Eq. (5) and associated ogive curves (Fig. 3). A 1-km overlapped moving window with an incremental step of 100 m was adopted, and data were assigned and averaged on 1-km contiguous

segments aligned according to the differentially corrected aircraft GPS position, resulting in an average flux value for each 1-km spatial segment per flight pass. Each spatially aligned 1-km flux segment was then averaged over all the flight passes resulting in an average flux for each 1-km segment over the entire flight campaign. The associated uncertainties, reported as error bars in the corresponding figures, are computed as the standard error of the mean (SEM) over all flight passes ($n = 29$).

Here, we use the micrometeorological convention with negative flux values representing uptake into the ecosystem from the atmosphere. The aircraft-based EC calculations and all footprint analyses were done using MATLAB (release 2006b, MathWorks, Natick, Massachusetts).

e. Portable tower-based eddy covariance

Portable tower-based ecosystem flux measurements were also done using the EC technique (Baldocchi et al. 1988; Loescher et al. 2006a,b; Swinbank 1951) with a portable tower system. The portable tower was located at the east edge of a large mangrove stand (25.259 83°N, 112.077 38°W) near the intersection between the DIA and the southern end of the MNG flight transects in Fig. 1 between 24 and 27 July 2004. This was a large contiguous mangrove stand with an upwind fetch of 750 m to the northwest and 800 m to the west before reaching the lagoon water. The mean canopy height of the mangrove at this stand was 3.5 m.

Measurements of the three-dimensional winds and virtual temperature were done with an ultrasonic anemometer (WindMaster Pro, Gill Instruments, Lymington, United Kingdom), while CO_2 and water vapor were also made using the same model of IRGA (LI-7500, LI-COR, Inc.) as on the aircraft. Incoming PAR (LI-190SB, LI-COR, Inc.), net radiation R_n with an aspirated Fritschen-type net radiometer (Q*7.1, REBS Inc.), air temperature T_{air} and relative humidity RH (HMP45c, Vaisala, Helsinki, Finland), ground heat flux G (HFT3, REBS Inc.), and soil temperature (Type-T thermocouples, Omega Engineering, Stamford, Connecticut) were also measured. An updated version of the program described in McMillen (1986, 1988; i.e., WinFlux, San Diego State University) was used to sample the portable tower-based turbulence parameters at 10 Hz with a 400-s time constant for the running mean and a digital recursive filter to estimate the turbulent fluctuations [Eq. (2)]. The slow response meteorological sensors were sampled at 10-s intervals and stored as half-hourly averages in a datalogger (23X, Campbell Scientific, Logan, Utah). Portable tower IRGA calibrations were done in concert with the aircraft IRGA calibration and followed AmeriFlux protocols (see above).

The sonic anemometer and the IRGA were located at a height of 4.2 m above the ground. The location of the net radiometer, air temperature, and RH sensors were over the mangrove stand while ground heat flux plates were placed 2 cm below the soil surface underneath the mangrove canopy and collocated with the soil temperature probes with measurements depths of 5, 15, and 20 cm below the soil surface.

Fluxes of CO_2, H, and λE were calculated as half-hourly averages and a 2D coordinate rotation was used to estimate the control volume and vertical wind velocities perpendicular to the mean streamline (Kaimal and Finnigan 1994; McMillen 1988). The fluxes were corrected for high-frequency losses in the measurement system due to inadequate scalar sensor dynamic response (Moore 1986), lateral sensor separation (Kristensen and Jensen 1979), sonic anemometer and IRGA line averaging (Gurvich 1962; Kristensen and Fitzjarrald 1984; Silverman 1968), and IRGA volume averaging (Andreas 1981), as well as for low-frequency losses from the running mean recursive filter (400 s) and the half-hourly block averaging (Kaimal et al. 1989; McMillen 1988; Moore 1986). We used the approach of Horst (1997, 2000) and Massman (2000, 2001) for calculating transfer functions based on atmospheric stability and the theoretical cospectral curves of Kaimal et al. (1972) described in Kaimal and Finnigan (1994). We used the equivalent time constants of first-order filters presented in Table 1 of Massman (2000) with the corrected equations in Table 1 of Massman (2001). Corrections for concurrent density fluctuations of heat and water vapor were done according to Webb et al. (1980).

Quality control included statistical checks for outliers of the CO_2 and water vapor measurements and the u, v, and w wind velocity components based on six standard deviations from their 30-min mean values, which were removed before the flux calculations. Wind directions were filtered so only winds coming from the mangrove stand to the west were considered. Fluxes were discarded when u_* was less than $0.25\,m\,s^{-1}$. This u_* threshold (Goulden et al. 1996; Gu et al. 2005) was determined when above a particular u_* the effect on the net ecosystem exchange (NEE) was unchanged and was similar to the u_* threshold of $0.21\,m\,s^{-1}$ used by Barr et al. (2010) for a mangrove ecosystem in the Everglades National Park, Florida. This u_* threshold was invariably associated with the nighttime and early morning low turbulence conditions and resulted in the rejection of 46% of the total fluxes and nearly 91% of the fluxes between 2200 and 0800 MST. Data gaps of 30 min or less were linearly interpolated (Falge et al. 2001), and gaps >30 min were filled using the online EC gap-filling and flux-partitioning tool (located at http://www.bgc-jena.mpg.de/~MDIwork/eddyproc/) that incorporates the techniques described in Falge et al. (2001) and using

TABLE 3. Flight line transect details and GPS endpoints using World Geodetic System 1984 (WGS84) for each flight transect. See Fig. 1 for visual representation of each transect over the study area.

Transect	Endpoint coordinates 1	Endpoint coordinates 2	Length (km)	Orientation
DIA	25.190 600°N, 112.201 843°W	25.305 484°N, 111.989 563°W	24.6	ENE–WSW
TNG	25.267 507°N, 111.996 474°W	25.282 829°N, 112.190 790°W	19.5	East–west
CST	25.311 325°N, 112.132 006°W	25.397 138°N, 112.115 517°W	9.3	North–south
MNG	25.398 526°N, 112.087 637°W	25.249 593°N, 112.078 126°W	16.3	North–south

enhanced algorithms that consider the temporal autocorrelation of fluxes and their covariation with meteorological variables as described in Reichstein et al. (2005). The energy balance and the degree of closure between the sum of the half-hourly H and λE ($H + \lambda$E) and the sum of R_n and G [$R_n + (-G)$] was used to determine system performance and the quality of the portable tower EC measurements (Aubinet et al. 2000; McMillen 1988).

f. Aircraft flight transects

Four flight transects were established to measure fluxes over the major ecosystems surrounding Lopez Mateos and are identified as CST, DIA, MNG, and TNG in Fig. 1 with the details of each transect available in Table 3. Transect DIA was a northeast–southwest orientated transect starting with the desert ecosystem from the east and extended over the mangrove and lagoon, a sandy barrier island, and ocean to the west. Flight paths along the DIA transect were directly over the portable EC tower upwind footprint located along the edge of a large mangrove stand. Transect TNG was east–west oriented and similar to DIA with desert to the east and ocean to the west, except that this transect also passed through the mouth of the Boca la Soledad. Transect CST was north–south along the coastline and made 7.3 m above the wave break zone, while the north–south MNG transect was made down the middle of the lagoon and flown over the mosaic of mangroves and surrounding lagoon waters. The DIA and the MNG transects intersect over the same mangrove stand where the portable EC tower was located with the aircraft passing within a 10- and 20-m horizontal separation at the nearest point from the portable EC tower, respectively. The aircraft followed the terrain as close to the ground as possible at an average measurement height of 8.48 m above all the surfaces with an average ground speed of 38.2 m s^{-1}. Multiple repeated passes were done to increase the sampling frequency and reduce the random flux error (Lenschow et al. 1994; Lumley and Panofsky 1964; Mahrt 1998; Mann and Lenschow 1994). All transects were flown as a continuous ''track'' with repeated passes flown in reciprocal directions. A complete reciprocal track took approximately 1 h, and most flights consisted of multiple passes with the total flight duration limited by the aircraft's fuel capacity (approximately 3.5 h). A total of 29 full tracks were flown during this campaign between the hours of 0530 and 1930 MST, with the flux measurement flights flown between 0930 and 1830 MST.

g. Flux footprints

To relate fluxes measured by tower and aircraft to their sink/source area on the ground, a footprint model was used to describe the contribution of the surface area to the measurement at a particular location (Kljun et al. 2002, 2004; Leclerc and Thurtell 1990; Schmid 2002; Schuepp et al. 1990). The flux footprint varies in size and depends on the measurement height above the surface, wind vector, surface roughness, and atmospheric stability (Leclerc and Thurtell 1990). Here, we used the footprint model of Kljun et al. (2004), which is a parameterization of a Lagrangian stochastic footprint model (LPDM-B; Kljun et al. 2002). The model described in Kljun et al. (2004) is a crosswind integrated footprint model that allows for rapid calculations with input parameters easily derived from common turbulence measurements. This footprint model requires the measurement height z, boundary layer height h, friction velocity u_*, standard deviation of the vertical wind σ_w, roughness length z_0, and the Obukhov length L (Foken 2006; Monin and Obukhov 1954; Obukhov 1946, 1971). The model is valid across a wide range of boundary layer stabilities and measurement heights with the overall conditions of $-200 \le z/L \le 1$, $u_* \ge 0.2$ m s^{-1}, and $1 \text{ m} < z < h$ (Kljun et al. 2004).

The footprint parameters for the portable tower EC system were calculated for the averaging period of the flux calculations (30 min), while the aircraft parameters were calculated from the spatial average of each measurement segment (1 km) along the flight paths. The z_0 can be derived from the logarithmic wind profile under neutral conditions from

$$u_z = \frac{u_*}{\kappa} \ln\left(\frac{z}{z_0}\right), \tag{7}$$

with u_z defined as the wind velocity at z and the von Kármán constant κ is 0.4.

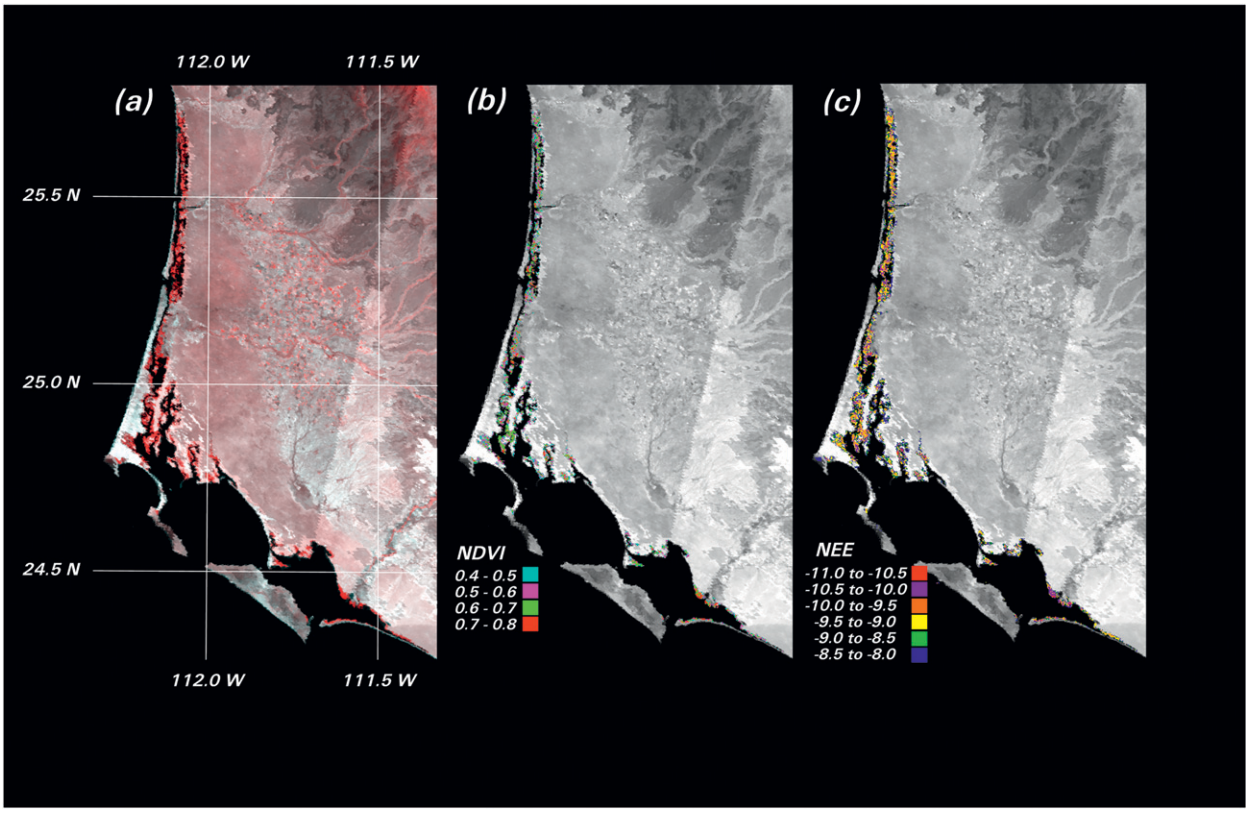

FIG. 4. Satellite imagery of the entire Magdalena Bay region derived from MODIS MOD09Q1 and aircraft data. (a) False color image using MODIS near-infrared spectral reflectance for red and MODIS red spectral reflectance for both green and blue image colors emphasize the mangroves and highlight vegetation density in increasing intensities of red due to the strong reflectance of near-infrared light by foliage. (b) The calculated mangrove NDVI based on the MOD09Q1 data and (c) mangrove CO_2 flux (μmol CO_2 m^{-2} s^{-1}) derived from the CO_2 flux and NDVI relationship determined by the aircraft measurements (see Fig. 7). Both (b) and (c) images use MODIS near-infrared spectral reflectance values as a grayscale background, with either calculated values of NDVI or CO_2 flux for the thematic color code overlay of the vegetated mangrove areas. The pixelation within the figure is the native pixelation of the MODIS image.

Flux footprints were calculated for each 1-km spatial block along each transect and evaluated to determine whether their surface sink/source area were either desert, mangrove, or ocean water. Respective ecosystems along each transect were then averaged to give the footprint estimations for each ecosystem. To compare the aircraft footprint to the portable tower footprint, the mangrove sections of the DIA and MNG transects that intersected the mangrove area measured by the portable tower were isolated from the surrounding ecosystems.

h. Determining regional mangrove coverage and NDVI

The NDVI is widely acquired from satellite- and aircraft-based platforms and recognized as an effective ecosystem-level indicator of plant health, primary productivity, and canopy capture of PAR (Box et al. 1989; Goward et al. 1991; Myneni et al. 1997; Sellers 1985; Tucker 1979; Vermote and Saleous 2006). Determination of regional-scale NDVI for the mangroves within the entire Magdalena Bay was done using the *Terra* satellite MODIS surface reflectance 8-day gridded level-3 global 250-m resolution data product, version 5 (MOD09Q1; http://modis-sr.ltdri.org/), managed by the MODIS Land Surface Reflectance Science Computing Facility (LSR SCF) (Vermote et al. 2002, 1997) and distributed by the Land Processes Distributed Active Archive Center (LP DAAC) located at the U.S. Geological Survey (USGS) Earth Resources Observation and Science (EROS) Center (https://lpdaac.usgs.gov).

Each MODIS MOD09Q1 pixel has the best possible observation during an 8-day period and provides MODIS b_1 and b_2 surface reflectance, which is corrected for atmospheric aerosol interference and high cirrus clouds (Vermote and Saleous 2006; Vermote and Kotchenova 2008; Vermote et al. 2002, 1997). The 5 min by 2300 km swath width MODIS image was subset spatially to approximately 350 pixels × 850 pixels or 80 km × 200 km to include only the Magdalena Bay area (Fig. 4). The most temporally appropriate dataset acquired for the

Magdalena Bay region was between 27 July and 3 August 2004. (The selected MODIS image was MOD09Q1.A2004209.h07v06.005.2010054222248.hdf, see https://lpdaac.usgs.gov/products/modis_overview for file description.)

The NDVI was calculated using the raw digital numbers in b_1 and b_2 from the LP DAAC MODIS product and scaled appropriately so all values are within the 16-bit signed integer image space. For our analysis and visualization of MODIS data, both MultiSpec (version 3.25.10, http://cobweb.ecn.purdue.edu/~biehl/MultiSpec/; Biehl and Landgrebe 2002) and ERDAS IMAGINE (2010, ERDAS Inc., Norcross, Georgia) software packages were used. A built-in IMAGINE function for NDVI calculation was used. The NDVI was added, for visualization purposes, as a third band in the image, and an analysis was made to determine if any generalizations regarding the ranges of NDVI within the known cover types could be made in the Magdalena Bay spatial subset. The known cover types of ocean, bay water, desert, mangroves plus water in mixed pixels, and homogeneous mangrove were identified by inspection of the three band image. An image displaying false-color IR was effective in determining vegetated areas (Fig. 4a). In this case, the MODIS band b_2 is displayed in the red, and band b_1 is displayed in both green and blue channels.

To characterize NDVI values representative of the five cover types, multiple rectangular samples, including only the desired cover type, were selected in MultiSpec and the NDVI values stored in a spreadsheet. To extract the NDVI values for all mangrove pixels, a series of rectangular selections were made along the entire length of the extant mangroves in the Magdalena Bay area, and each selection of pixels was saved for further analysis. The extractions were made to exclude as many nonmangrove pixels as possible since all selected pixels had to be screened for appropriate NDVI range, and the out-of-range pixels were excluded prior to summation and further processing. The total number of pixels within the mangrove NDVI range of 0.3–0.8 was summed and multiplied by the area of each pixel to determine the total mangrove ecosystem area.

Since these values were from individually selected single pixels of known cover type, we chose to broaden our analysis of the mangrove-only pixels. For further analysis of the mangrove areas, we sampled all pixels within the mangroves. This more extensive sampling included some full-canopy mangrove samples and various mixtures of canopy and water or canopy and land, water, and even bare soil. The individual pixel values were extracted from the IMAGINE-derived NDVI image and nonvegetated pixels (NDVI ≤ 0.0) were removed as well as any pixels that had NDVI values greater than any observed in the pixel-by-pixel analysis (NDVI > 0.79). Based on the spherical projection of the MODIS MOD09Q1 image, each pixel was 231.66 m $\times$ 231.66 m or 53 666.4 m^2.

3. Results

a. Aircraft system performance

The specified series of in-flight calibration maneuvers were used to determine the empirical values of calibration constants of the wind computational model (Bögel and Baumann 1991; Kalogiros and Wang 2002a; Khelif et al. 1999; Leise and Masters 1993; Lenschow 1986; Lenschow et al. 2007; Telford et al. 1977; Tjernström and Friehe 1991; Vellinga et al. 2013; Williams and Marcotte 2000). Complex flight maneuvers such as constant altitude standard rate turns ($3° s^{-1}$) and wind boxes were used to evaluate the results of the calibration of the aircraft's wind vector system and postprocessing routines (Telford and Wagner 1974; Telford et al. 1977; Vellinga et al. 2013). A constant altitude standard rate 450° counterclockwise turn flown during the calibration flight on 28 July 2004 at 1560 m ASL was assessed to verify the quality of the calibration. During an aircraft turning maneuver or circular flight path, both V_p and V_a are continuously changing and errors in either of these measurements manifest in errors of V. Since no biases were observed in either V_p or V_a, the resulting velocity of V was nearly constant throughout the entire 450° turn. The measured velocity of V during this turning maneuver was $3.45 \pm 1.05\ m\ s^{-1}$ with a measured wind direction of 264° ± 2.38° true.

The ogive plots for Co_{wCO_2} of all the flight legs over the DIA and MNG transects show a convergence and asymptotic shape of the ogive functions at low frequencies suggesting that all flux-carrying turbulence scales are captured within the length of the transects and can be used to robustly determine the spatial averaging scales (Fig. 3). An averaging length of 1 km was used as the optimal averaging length for the subsequent EC calculations. Ogive functions for the CST and TNG transects also showed similar shapes and convergence toward a spatial averaging length of 1 km (data not shown).

b. Flux footprints

The results of the footprint analysis for the aircraft and portable tower are presented in Table 1. Overall, the average maximum footprint contribution area x_{max} and the 90% flux contribution distance $x_{90\%}$ were largest over the ocean, 110.7 and 303.2 m, respectively. As expected, the z_0 was lowest over the ocean and highest over the desert, which had a x_{max} and $x_{90\%}$ of 94.8 and 259.6 m, respectively. The footprint over the mangroves

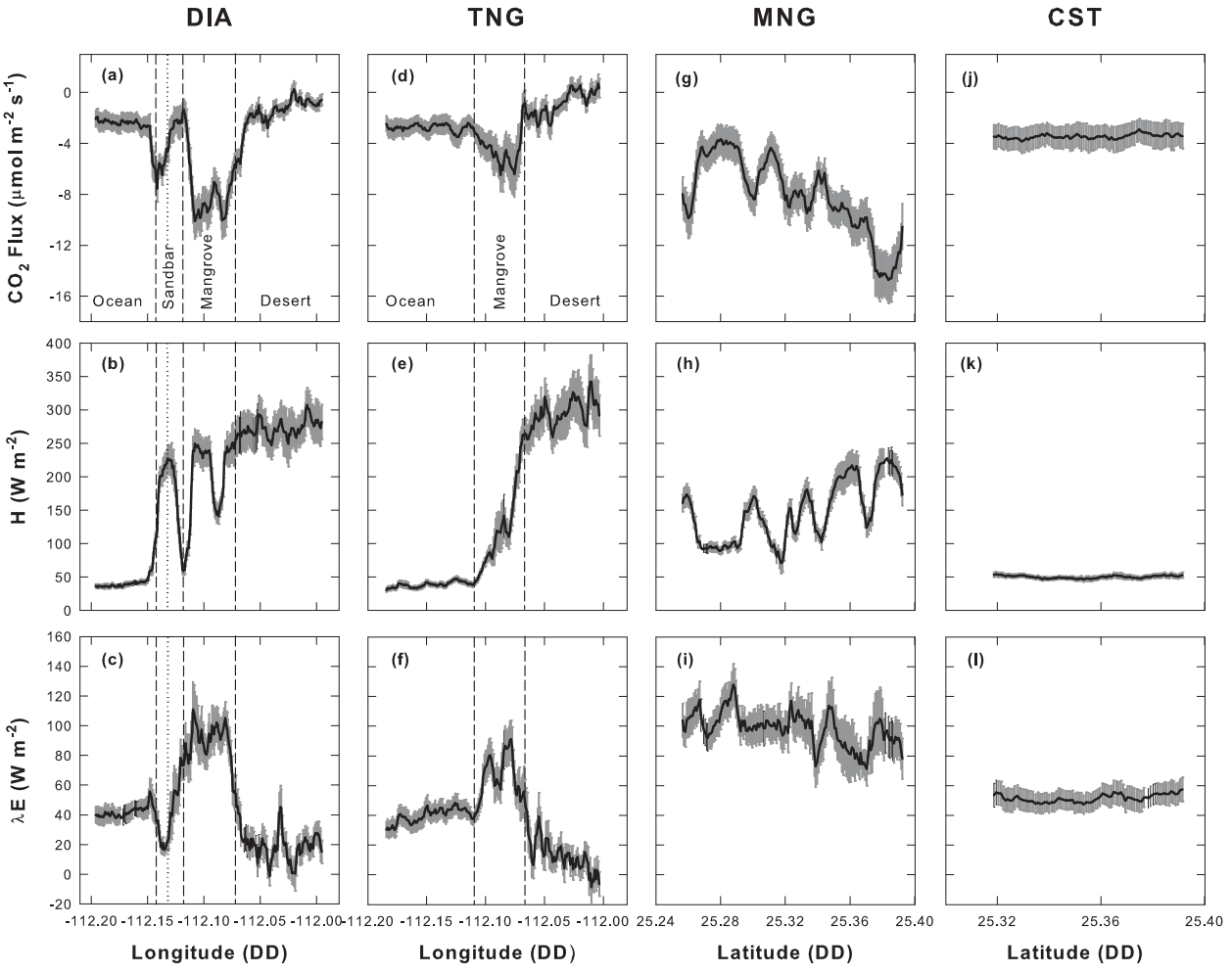

FIG. 5. Average fluxes of CO_2, H, and λE across the DIA, TNG, MNG, and CST aircraft flight transects (see Fig. 1). The dashed vertical lines indicate ecosystem boundaries and the dotted line indicates the sandy barrier island. The closest approach of the aircraft to the portable EC tower along the DIA and MNG transects were 10- and 20-m horizontal separation, respectively. Shading indicates the SEM.

were a mix of continuous mangrove stands and open lagoon water and had an average x_{max} of 73.9 m and $x_{90\%}$ had an average of 217.1 m. The aircraft footprints, x_{max} and $x_{90\%}$, for the mangrove area where the portable tower was located were 5 times larger than the footprint of the portable tower, mainly because of the differences in measurement height between the portable tower and aircraft, 4.2 and 7.98 m, respectively.

c. *Aircraft-measured spatial variability of fluxes and NDVI*

The DIA and TNG transects cross over the various ecosystems from the desert in the east, the mangrove and lagoon system in the middle, and the ocean to the west (see Fig. 1). The dashed lines in Fig. 5 demark the boundaries of the different ecosystems along the DIA and TNG transects. The DIA transect crosses over a sand-covered barrier island between the mangrove lagoon and the ocean, while the TNG transect crosses through the mouth of the Boca la Soledad. The CST and MNG transects were oriented north–south with the CST over the nearshore coastline just over the wave break zone and the MNG down the middle of the mangrove and lagoon area (see Fig. 1). Differences in the fluxes of CO_2, H, and λE are clearly observed from the different ecosystem types/source areas in the DIA and TNG transects (Fig. 5).

The mangrove ecosystem had the largest CO_2 uptake with an average flux of $-8.11\,\mu\text{mol}\,CO_2\,m^{-2}\,s^{-1}$ with a maximum rate of $-14.7\,\mu\text{mol}\,CO_2\,m^{-2}\,s^{-1}$ over a large mangrove stand located between the desert and lagoon (the DIA transect and the southern end of the MNG transect). The average CO_2 flux of the desert ecosystem was small with an average uptake of $-1.32\,\mu\text{mol}\,CO_2\,m^{-2}\,s^{-1}$, while the coastline and nearshore ocean had uptake rates of $-3.48\,\mu\text{mol}\,CO_2\,m^{-2}\,s^{-1}$.

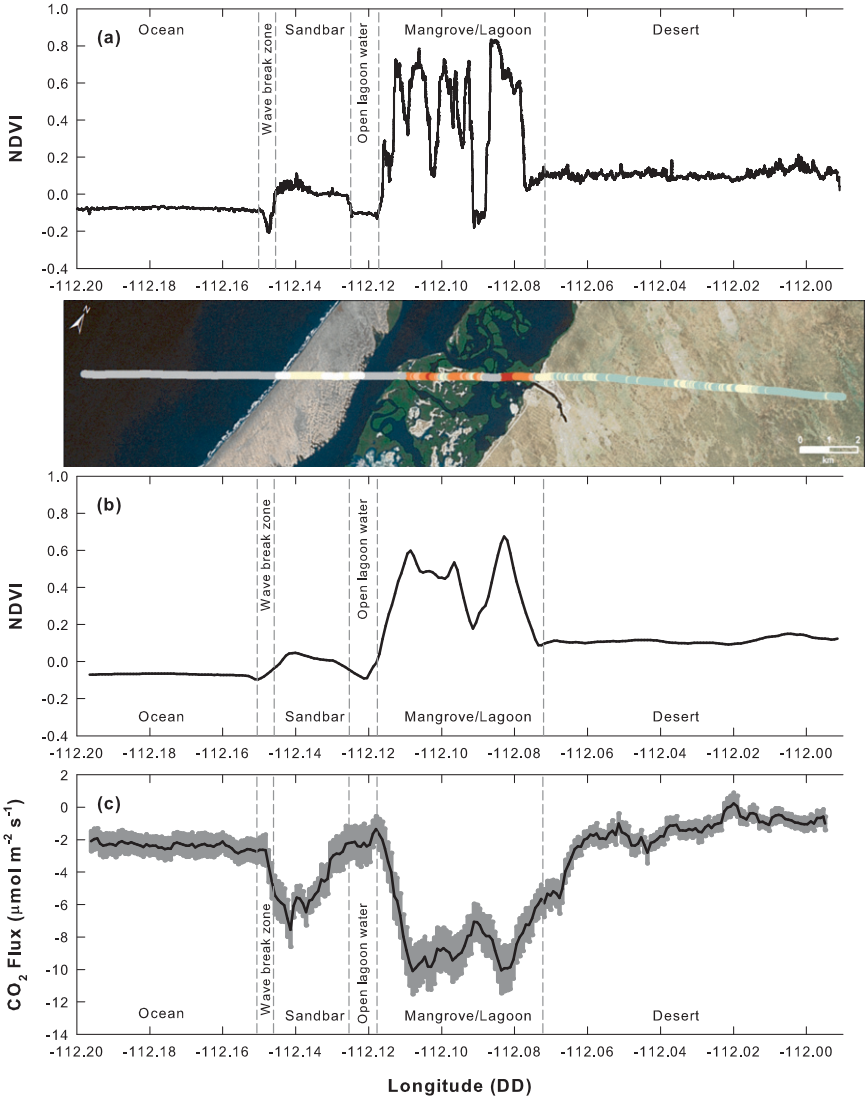

FIG. 6. CO_2 flux and NDVI along the DIA transect. (a) High spatial-resolution NDVI measurements from the aircraft can distinguish finescale differences in surface type; however, since the aircraft cannot resolve fluxes less than the spatial averaging block (1 km), the high-resolution NDVI is averaged with the same (b) 1-km spatial block as (c) the CO_2 flux. The map is presented to show the correspondence of the NDVI and CO_2 flux to the surface along the DIA transect. Shading in (c) indicates the SEM.

Average H was highest over the desert at 282 W m^{-2}, while the ocean had the lowest H at 50.4 W m^{-2}. The MNG transect had the largest range in H, from 59.7 to 249 W m^{-2}, which depended on whether the flight path was over a mangrove stand (high H) or lagoon water (low H). Small mangrove stands were interspersed within the lagoon area, which resulted in the pattern of H seen in Fig. 5h. Latent heat was highest over the mangroves (88.0 W m^{-2}) and lowest over the desert (17.6 W m^{-2}), with the near shore and ocean consistently at 44.3 W m^{-2}.

We were able to detect differences in NDVI among the various ecosystems and surface features with the ability to resolve even narrow ecosystem borders (see Figs. 1, 6a). Borders between the ocean and lagoon waters were also distinguishable. The high-resolution hyperspectral measurements were averaged to a 1-km spatial resolution (Fig. 6b) to match the spatial resolution of the aircraft fluxes (Fig. 6c) for comparisons between NDVI and NEE (Fig. 7).

The NDVI over the mangroves were the highest and most variable, 0.05–0.7, while the desert was consistently

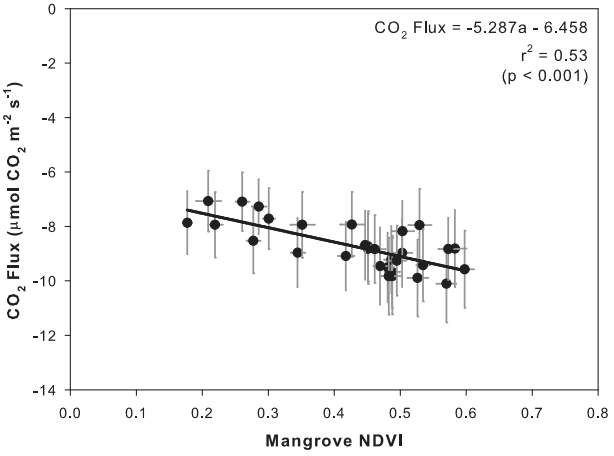

FIG. 7. Comparisons of CO_2 flux and NDVI along the mangrove-covered sections along the DIA transect. There is an increase in the CO_2 uptake of the mangroves with increasing NDVI. Vertical and horizontal bars indicate SEMs.

low, 0.09–0.15. The range of NDVI within the desert was small, and there was no relationship found between CO_2 flux and NDVI, while CO_2 flux over the mangroves showed increased uptake with higher NDVI (Fig. 7). The highest NDVI recorded was over the large homogeneous mangrove stand where the portable tower was located (see Fig. 1), while low NDVIs were typically found from a mixed measurement of mangrove and lagoon water or areas dominated by sand.

d. Portable tower-based mangrove flux measurements

The average diurnal pattern of CO_2 flux, energy balance, PAR, and T_{air} for the large mangrove stand between 24 and 27 July 2004 is shown in Fig. 8. Low turbulence and stable atmospheric conditions prevented calculations of fluxes from 0230 to 0730 MST; however, by 0800 MST the mangrove stand showed strong CO_2 uptake coincident with a PAR of about 800 μmol m^{-2} s^{-1}. An average maximum uptake rate of -12.3 μmol m^{-2} s^{-1} persisted from 0830 to 1330 MST with a peak uptake of 13.5 μmol CO_2 m^{-2} s^{-1}. There was a steady decline in CO_2 uptake from 1400 to 1730 MST, and by 1800 MST the mangrove ecosystem switched from uptake to CO_2 efflux, though the PAR was still relatively high (about 800 μmol m^{-2} s^{-1}). Nighttime CO_2 flux was consistent and averaged 3.97 μmol CO_2 m^{-2} s^{-1}.

The energy balance closure for the portable EC tower was 75% with the slope of the regression between the sum of the half-hourly $H + \lambda E$ and $R_n - G$ at 0.88 with an $r^2 = 0.91$, indicating a small underestimation in $H + \lambda E$. We had good energy balance closure when compared with other FLUXNET (Baldocchi et al. 2001)

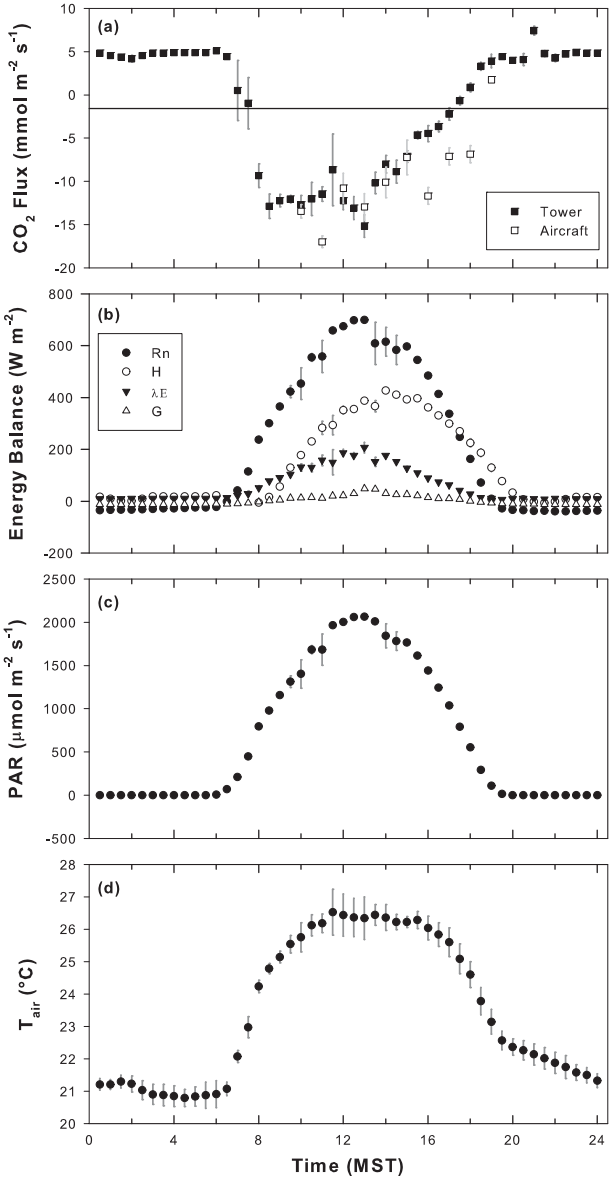

FIG. 8. Portable tower measurements of (a) CO_2 flux, (b) surface energy balance, (c) PAR, and (d) T_{air} (see Fig. 1 for tower location). A comparison of tower- and aircraft-based EC CO_2 flux is presented in (a). Vertical bars indicate SEMs.

sites (Wilson et al. 2002). The R_n was typically symmetrical from the peak of 699 W m^{-2} occurring at midday (1300 MST). The λE had a similar pattern to R_n with a coincident peak time frame and a maximum of 229 W m^{-2}. The H typically lagged R_n and λE and peaked between 1330 and 1400 MST at 435 W m^{-2}. Ground heat flux was not particularly large even during the midday with a peak of 48.2 W m^{-2}. Values of R_n, H, and G were typically negative at night and early morning from 1930 to 0700 MST. The pattern of incoming PAR was also symmetrical from the midday peak of

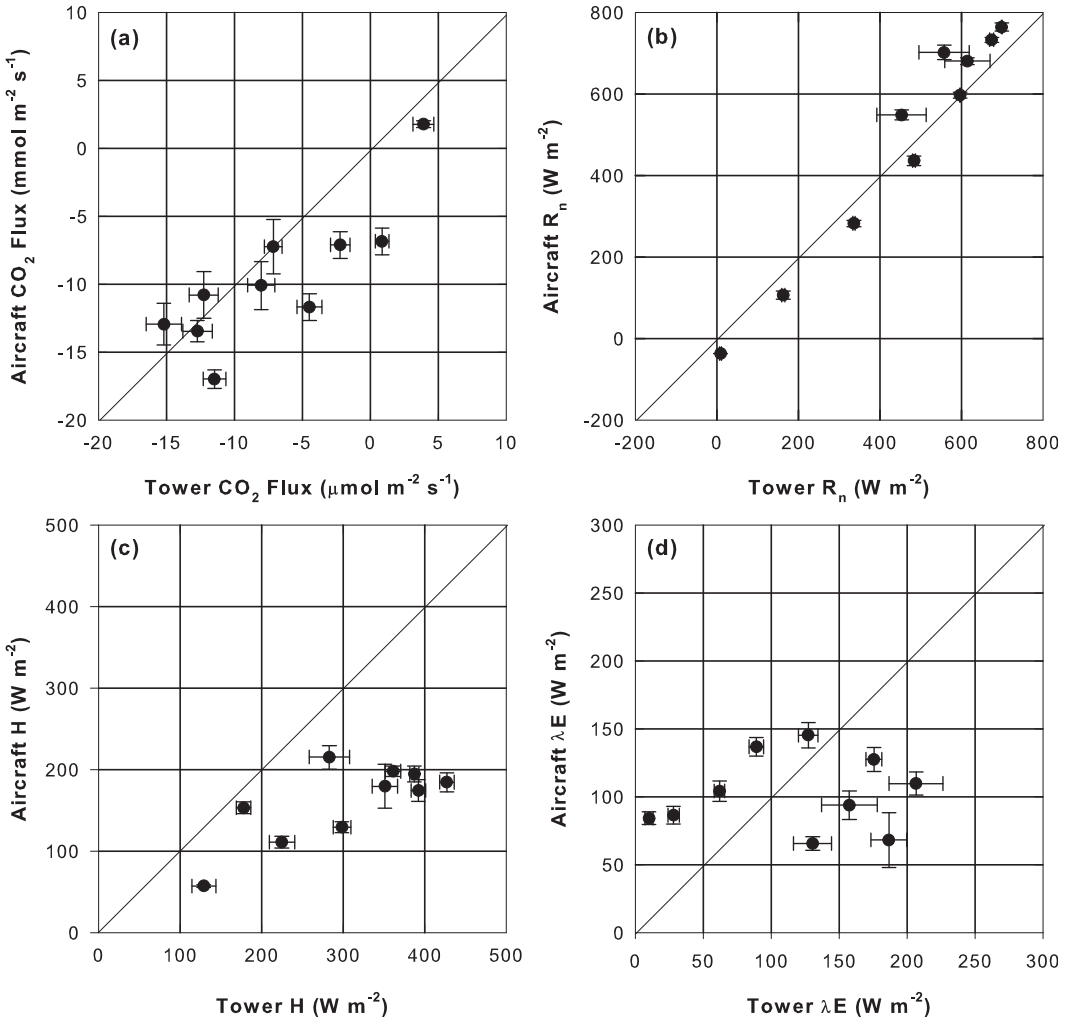

FIG. 9. Intercomparison between the portable tower and the aircraft over the same mangrove stand along the DIA and southern end of the MNG transect (see Fig. 1 for tower location). Aircraft data are 1-h bins of 1-km spatial blocks corresponding to the time of passage past the portable tower. The portable tower data are binned accordingly by matching times. The solid diagonal line is the 1:1 line, and vertical and horizontal bars are the SEM.

2064 μmol m^{-2} s^{-1} with nighttime darkness from about 1930 to 0600 MST, coinciding with local sunset (1917 MST) and sunrise (0553 MST), respectively (http://www.esrl.noaa.gov/gmd/grad/solcalc/). Air temperature was lowest just before sunrise and rose rapidly with maximum temperatures, about 26.3°C, extending from 1030 to 1630 MST, followed by a nearly linear decline from 1930 MST to around midnight.

e. Portable tower and aircraft intercomparison

To compare the portable tower- and aircraft-based EC measurements, we isolated the 1-km spatial averaging block of the aircraft along the DIA and MNG transects within the fetch of the mangrove stand measured by the portable tower. This was done for all the passes of the DIA and MNG transects. The 1-h bins were created with each bin centered on the hour and all the flight passes were placed into corresponding bins depending on their time of passage past the portable tower. These were then averaged and the SEMs were determined. All the portable tower data were treated similarly by binning matching times together over the entire campaign. Each hourly portable tower bin corresponding to the aircraft measurements is compared. The intercomparison between the tower and aircraft is shown in Fig. 9. There was good agreement in R_n between the aircraft and tower (Fig. 9b) with a slope of 1.21 and an $r^2 = 0.96$, showing that the aircraft R_n over this mangrove area was slightly larger compared to the ground-based measurements. Compared to the tower, the aircraft underestimated the CO_2 flux (Fig. 9a) by 25% with a slope of 0.75 and an $r^2 = 0.74$. There was an

underestimation of the tower H by the aircraft with a slope of 0.36 and an $r^2 = 0.55$ (Fig. 9c), while the variance in the aircraft λE could not be explained by variations in the tower λE (Fig. 9d).

f. Aircraft-derived temporal patterns

The multiple flights throughout this campaign occurred between sunrise and sunset with the concentration of the flux flights occurring between 0930 and 1830 MST. Aggregating the times, locations, and separating out the various ecosystems for the entire campaign, it was possible to use the aircraft to obtain a temporal flux pattern throughout the day among the studied ecosystems (Fig. 10). The aircraft-derived temporal patterns of CO_2 flux over the mangrove areas (Fig. 10e) were consistent with that from the portable tower in magnitude, direction, and pattern (see Fig. 8a). Though both H and λE estimates were less than those found by the portable tower (Figs. 9c,d; i.e., lower magnitudes), the overall diurnal pattern remained consistent between the tower and the aircraft.

g. MODIS regional mangrove coverage and NDVI

The NDVI values for the five cover types are presented in Table 4. With the larger amount of sampled mangrove areas, the range of NDVI of mangrove-dominated pixels was 0.300–0.800. Based on this NDVI range, there were 6731 pixels making up 361.23 km^2 of mangrove-dominated areas in the area of analysis. Using the MODIS-derived NDVI and NEE relationship derived from the aircraft flights (Fig. 7) with all the NDVI mangrove pixels (Fig. 4b), we calculated the NEE for each pixel and summed them for a total mangrove ecosystem CO_2 flux. Based on the number of mangrove-identified MODIS pixels, NEE ranged from $-8.0\,\mu mol\,CO_2\,m^{-2}\,s^{-1}$ with an NDVI of 0.300 to $-10.7\,\mu mol\,CO_2\,m^{-2}\,s^{-1}$ for the highest NDVI value of 0.800. Fully scaled to the number of mangrove-identified MODIS pixels and weighted by NDVI, the midday average CO_2 flux was $-9.2\,\mu mol\,CO_2\,m^{-2}\,s^{-1}$, and the sum of all the pixels was over 361.23 km^2; the areal midday NEE was $-526.27\,t\,CO_2\,h^{-1}$ throughout the Magdalena Bay region.

4. Discussion

a. Ecosystem fluxes

In the Magdalena Bay region the distinct borders among ecosystems over small spatial distances (see Fig. 1) and the contrast among the desert, mangrove, and lagoon ecosystem fluxes of CO_2 is dependent on the time of year. During the summer months, the desert ecosystems of BCS have low productivity or are small sources of CO_2 to the atmosphere because of the relatively small amounts of biomass, high temperatures, solar radiation, and low water availability (Bell et al. 2012; Hastings et al. 2005). However, desert ecosystems are not completely devoid of photosynthetic activity and drought resistant desert evergreen species such as *L. tridentata* and *S. chinensis*, bark photosynthetic species such as *Cercidium microphyllum* and *Fouquieria splendens*, and succulent species such as *P. pringlei*, *S. thurberi*, and *O. cholla* do persist and can be productive even throughout the summer months. Though photosynthetic activity is reduced by drought conditions and high temperatures, and by drought-induced loss of leaves from drought deciduous species and annual grasses, CO_2 uptake has been shown to occur in a similar desert scrub community outside of La Paz, BCS, Mexico, particularly in the early and midmorning hours (Bell et al. 2012; Hastings et al. 2005). Desert ecosystems are also reported to have significant CO_2 uptake annually as well as during the summer months (see, e.g., Wohlfahrt et al. 2008). Photosynthesis may often offset ecosystem respiration; however, during extended summer droughts, desert ecosystems have been shown to be an annual net source of CO_2 to the atmosphere (Bell et al. 2012; Hastings et al. 2005). This net CO_2 source during the summer can persist even after a precipitation event where the microbial biota can respond more quickly to small amounts of water from summer precipitation events than can the annuals and drought deciduous species (Huxman et al. 2004; Reynolds et al. 2004; Sponseller 2007). However, major precipitation events, such as hurricanes and tropical storms, coincide with the maximum productivity of these desert ecosystems (Bell et al. 2012; Hastings et al. 2005; Huxman et al. 2004; Knapp and Smith 2001) because of the cooccurrence of moderated temperatures and increased water availability; however, these events occur mainly during the fall and winter months.

The mangroves during the summer months are at their peak of productivity (Chavez 2006; Osborne 2000) with peak measured NEE during the middle of the day. Though the mangrove trees have an apparent abundance of water, they are under water limitation because the highly saline lagoon waters caused them to develop physiological coping mechanisms, which give them high water-use efficiency (Alongi 2009). The combination of high solar radiation, warm temperatures, and abundant nutrient availability results in the high productivity of these mangrove ecosystems (Alongi 2009).

Here, aircraft-based EC measurements (i) demonstrate a net CO_2 uptake for a large homogeneous mangrove stand with the validation of both direction and the magnitude of the flux from the portable tower-based measurements and (ii) differentiate different sources

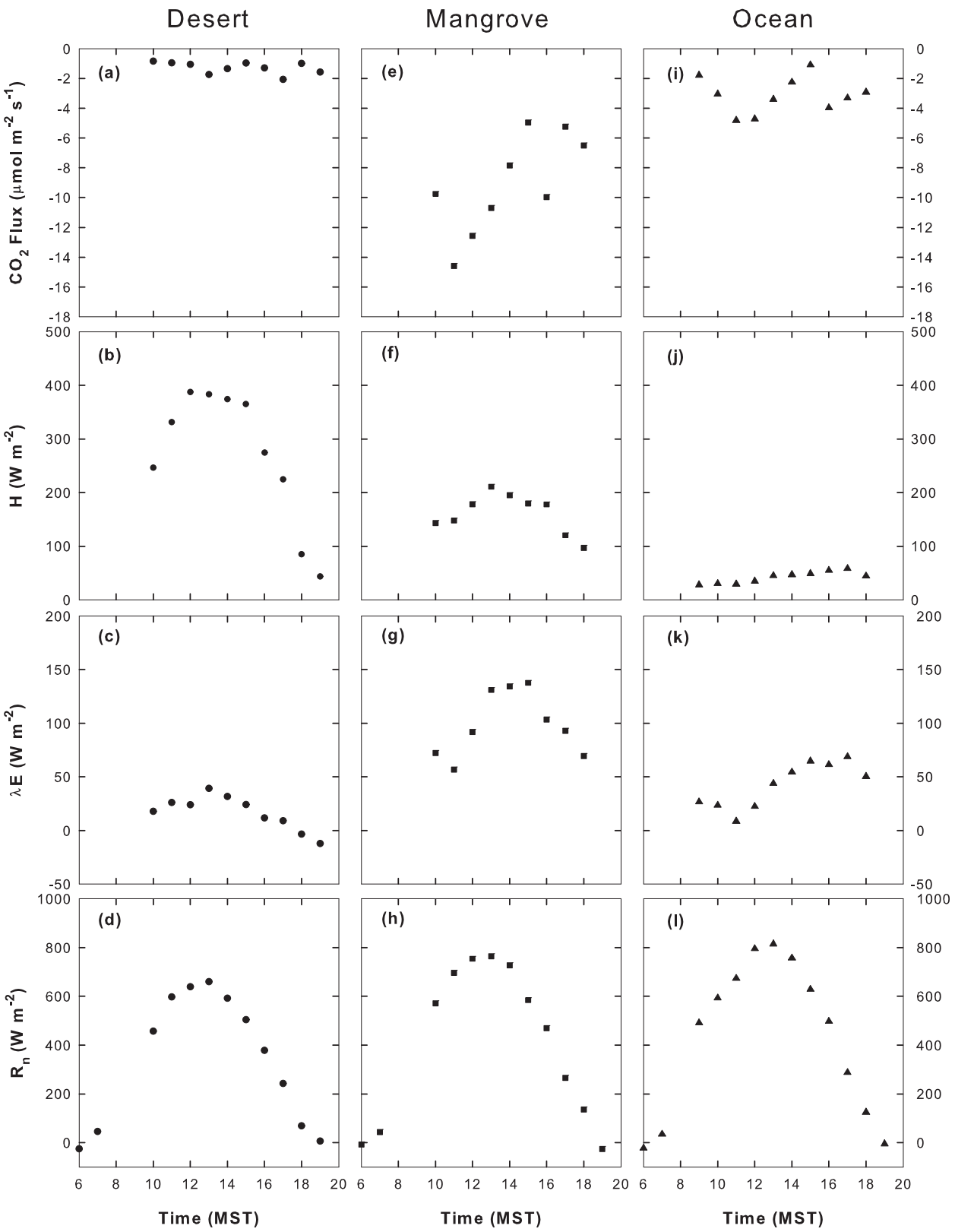

FIG. 10. Aircraft-derived temporal patterns of CO_2 flux, H, λE, and R_n along the desert, mangrove, and ocean sections of all flight transects.

TABLE 4. NDVI statistics for five cover types within the Magdalena Bay region calculated from a single MODIS MOD09Q1 8-day composite 250-m bands b_1 and b_2 image. Pixels were selected through visual identification of the cover type and manual sampling of multiple pixels within those cover types using MultiSpec (Biehl and Landgrebe 2002). Clouds, fog, or sunglint precluded the use of many water-dominated pixels.

		NDVI		
Cover type	No. of discrete pixels	Avg	Min	Max
Ocean	19	−0.727	−1.00	−0.514
Bay water	1590	−0.825	−1.00	−0.013
Desert	3520	0.209	0.151	0.260
Mangroves + water	42	0.584	0.469	0.790
Homogeneous mangrove	69	0.635	0.463	0.757

areas (i.e., open water, mangrove, lagoon, and desert ecosystems). Though we did not specifically measure the fluxes from the lagoon itself (tower based or surface layer based), a subsequent study measured the differences in the CO_2 partial pressure (Δp_{CO2}) between the atmosphere and the lagoon surface waters (just north of Lopez Mateos) with a shower equilibrator (Broecker and Takahashi 1966) and a nondispersive IRGA (LI-840, LI-COR Inc.) that showed the lagoon to be a source of CO_2 to the atmosphere (Ikawa 2012). This corresponds with previous reports that lagoon waters surrounding mangrove forests are small but net CO_2 sources (Borges et al. 2003). Since the aircraft integrates fluxes from mangrove and lagoon over the 1-km spatial average, the integration of the mangrove and lagoon flux signals will show variable and typically smaller NEE rates when compared to the mangrove stands with little or no standing water. However, because of the very high productivity of the mangroves, daytime NEE exceeds ecosystem respiration; the mangrove–lagoon complex was still a significant net CO_2 uptake. Barr et al. (2010) reported maximum daytime uptake rates from -20 to $-25\,\mu$mol $CO_2\,m^{-2}\,s^{-1}$ of a large stature mangrove forest in the western Everglades National Park, nearly 2 times the maximum uptake rates reported here.

The nearshore ocean CO_2 uptake is likely due to several factors, which include nutrient outflow from the bay and coastal upwelling of deep nutrient rich waters. This study is consistent with other studies of nearshore ocean uptake of CO_2 (Cai et al. 2006; Hales et al. 2005). The aircraft measurements showed an uptake of CO_2 along the coastline, and if the flight transect was extended farther into the Pacific, we would have been able to determine the extent of the nearshore uptake. It is also important to note that increased CO_2 uptake at the shore break may be due to increased air–sea exchange through bubble entrainment (Asher et al. 1996; Farmer et al. 1993; McNeil and D'Asaro 2007; Zhang et al. 2006). This airborne technique can be used to elucidate the ecosystem processes at the terrestrial–coastal–ocean interface, which have been receiving increasing attention in both advances in science and in policy (Vargas et al. 2012).

b. Tower and aircraft intercomparison

Proper planning of tower sites and flight paths ensure favorable comparisons between tower and aircraft measurements over relatively homogenous sampling areas (e.g., Zulueta et al. 2011). However, even the most carefully planned sites and campaigns have limitations for direct tower and aircraft intercomparisons. Since aircraft-based EC measurements integrate over large spatial areas and are in constant transition across the landscape, footprint mismatches and different-averaging temporal and spatial scales make direct comparisons between tower and aircraft challenging to interpret. Conceptually, the aircraft footprint is a moving and continuously integrating swath of the upwind landscape with approximate dimensions equal to the footprint length times the distance of each measurement block, and therefore several times larger than the tower footprint even if the aircraft was flown at the same height as the tower.

Moreover, because the aircraft transits across the landscape, its footprint for each averaging block are a ''snapshot'' of the upwind source area while the tower footprint is sampling continually over a typically better defined and constrained area. The temporal and spatial scales from these two approaches still can be linked to make comparisons.

Intercomparisons between aircraft- and tower-based EC measurements have been made in previous studies over a range of different ecosystems (Crawford et al. 1993b, 1996b; Desjardins et al. 1989, 1992; Gioli et al. 2004; Isaac et al. 2004; Kelly et al. 1992; Oechel et al. 1998; Zulueta et al. 2011) and the results presented here are consistent with those studies. An early study using data from the 1987 First International Satellite Land Surface Climatology Project (ISLSCP) Field Experiment (FIFE) campaign (Kelly et al. 1992) found aircraft measurements of H to be 20%–50% lower than the ground-based measurements, and aircraft measurements of λE were lower than the ground-based measurements at high-λE and greater at low-λE values. Desjardins et al. (1992) in an analysis of the National Research Council (NRC) Twin Otter data from the 1987 and 1989 FIFE campaigns found H and λE in agreement at the University of Nebraska-Lincoln (UNL) site for both years, but at

the Argonne National Laboratory (ANL) site the aircraft underestimated H by about 40% in both years and overestimated λE by about 14% in 1989. A later study by Crawford et al. (1996a) found aircraft measurements underestimated H by 10%–20% and overestimated λE by 25%, while Desjardins et al. (1997) also found that aircraft measurements underestimated H and overestimated λE, but the sum of $H + \lambda E$, however, were comparable to the ground-based measurements. In general, these earlier aircraft–tower intercomparisons found that aircraft measurements of H were less than surface-based measurements by 10%–50% with mixed results for λE. Fluxes of CO_2 were not always measured in these studies; however, a study with this particular Sky Arrow and instrumentation package and a pair of portable EC towers over a homogeneous upwind surface area showed a near 1:1 relationship between the aircraft- and tower-based CO_2 fluxes with slight underestimations of H and λE (Zulueta et al. 2011). The Sky Arrow platform resolved different surface processes and ecosystem types across the Arctic landscape providing the observations that facilitated spatial scaling approaches (Zulueta et al. 2011). With this study and others found elsewhere, we have high confidence in our ability to denote ecosystem boundaries and hence also in determining our source areas. The future of linking these approaches can be used for more complex spatial data assimilation approaches for larger areal estimates, to identify terrestrial–ocean interfaces, and be used for targets of opportunity (e.g., flooding, fires, and land use changes).

Flux measurement sites are typically selected within predominant or ecologically important ecosystems within a region. Careful attention is put toward the representativeness of a site for a certain area and usually within as structurally and functionally homogeneous an ecosystem as possible. However, even ecosystems considered homogeneous, such as deserts, mangroves, and the Arctic tundra, show a large degree of spatial variability in structure and function over short distances of kilometers or less (Hinkel et al. 2001; Riedel et al. 2005; Shaver et al. 1996; Vourlitis et al. 2003; Walker et al. 1994). In areas where an ecosystem is heterogeneous or where multiple ecosystems converge, such as the complex coastal ecosystem of Magdalena Bay, selecting a site with a representative source area is clearly difficult, and a bias in site selection can lead to biases in scaling flux estimates to the region if only tower information is used (Kelly et al. 1992). The ability to differentiate various landscape features from aircraft-based measurements in terms of their surface fluxes have been demonstrated here as well as across a range of different ecosystems from grasslands (Desjardins et al. 1992; Gioli et al. 2004; Kelly et al. 1992), broadleaf, evergreen, and boreal forests (Crawford et al. 1996b; Gioli et al. 2004), agricultural fields (Desjardins et al. 1989; Gioli et al. 2004; Isaac et al. 2004), Arctic tundra (Brooks et al. 1996; Oechel et al. 1998; Zulueta et al. 2011), and subtropical coastal environments (Crawford et al. 1993b). Whereas towers are limited in spatial area coverage, aircraft have the ability to measure across large expanses of landscape and, in this case, aircraft flux measurements may be more accurate an assessment of the landscape or regional fluxes than extrapolating solely from tower-based measurements. However, aircraft are limited in temporal coverage and measurements tend to be biased as flight regulations and safety limit aircraft flights to daylight hours or ''good'' weather conditions. The aircraft- and tower-based flux measurements are therefore complementary and combined provide for both a temporal and spatial assessment of surface fluxes and a means for improved landscape and regional scaling.

c. Toward regional-scale flux estimates

Measurements of regional-scale surface fluxes (at scales of hundreds of square kilometers) and validation of remotely sensed satellite data products and model outputs are necessary to understand the processes that determine a region's influence on local and global carbon budgets and climate (Desai et al. 2010; Dolman et al. 2009). Numerous measurements of landscape-scale EC fluxes are actively underway globally through the collaborative efforts of FLUXNET (Baldocchi et al. 2001). However, despite the hundreds of towers within the FLUXNET community, the majority is located within the Northern Hemisphere and temperate climates (Williams et al. 2009) and even these are neither randomly nor uniformly distributed. Their locations were not decided in a coordinated effort to facilitate the spatial scaling of fluxes. Therefore, the spatial density of representative flux towers is still relatively sparse, and the range of spatial variability is inadequately sampled to scale with confidence from ecosystem to landscape to region to continent. This is particularly true in harsh environments and/or remote areas such as semiarid, arid, desert, tropical, and Arctic ecosystems. In many of these areas, infrastructure is limiting and challenging logistics make flux measurements not easily obtainable. The mismatch between the chamber and tower scales of measurement and a mismatch between ecosystem-level scales and modeled grid size estimates of fluxes, along with the inability to determine mechanistic linkages among these scales, have remained a major impediment to validating model algorithms and outputs as well as to quantifying regional carbon fluxes with confidence.

Nonetheless, regional estimation of fluxes, including those in remote areas, can be improved by the aircraft

methodology presented here. This methodology is an effective bridge from plot to ecosystem to regional scales and for use in extrapolation, interpolation, and model and satellite verification (Beringer et al. 2011a; Desjardins et al. 1997; Oechel et al. 2000; Ogunjemiyo et al. 1997) and can be used to establish baseline measurements that can be coupled with satellite-derived data products.

The region may have surface and landscape features with much finer spatial scales than the minimum resolvable flux scale of the aircraft (1 km); however, the integrated nature and continuous spatial coverage provide by the aircraft are valuable in assessing the spatial variability across much larger spatial areas than towers alone. The spatial variability of fluxes among these complex coastal ecosystems outlines the importance of the need for measurements that can sufficiently cover the regional spatial variability. The validation of satellite data and model outputs in this ecosystem would be problematic, if not biased, if based on extant and typical tower flux values and locations. A common method of validation of modeled or satellite-derived data is from the point measurements from EC tower sites (Heinsch et al. 2006; Sasai et al. 2005; Sasai et al. 2007; Sims et al. 2006; Turner et al. 2005), and an intensive validation of the MODIS data products have been undertaken with the goal to improve the MODIS algorithms (Cohen et al. 2003; Turner et al. 2005). Even though tower-based measurements are temporally explicit, their spatial coverage is quite small compared to MODIS products, resulting in significant data gaps to scaling from tower-based to regional- and global-scale estimates.

There is an increased need to scale ecological processes and their abiotic drivers to larger and larger spatial scales for use in ecology, as well as for the use of policymakers (National Research Council 2001, 2003). Advancing scaling strategies is central to new emerging ecological networks (Marshall et al. 2008; Peters et al. 2008; Schimel et al. 2011), and multidisciplinary campaigns like CarboEurope Regional Experiment Strategy (CERES; Dolman et al. 2006, 2009) and Savanna Patterns of Energy and Carbon Integrated Across the Landscape (SPECIAL; Beringer et al. 2011a,b) have been initiated using similar technologies and methodologies as presented here. Use of light aircraft for near-surface EC flux estimates increases the spatial sampling density from tower-based footprints to larger areas and used in conjunction with towers, remotely sensed products, and ecosystem models enables a better understanding in the patterns and controls on regional fluxes. Even at micrometeorological ideal tower sites (even-aged stands and long flat homogeneous vegetation/fetch), assumptions of homogeneous scalar source/sink strength and local circulations are questioned (Loescher et al. 2006a). Aircraft-based measurements, while limited in temporal scale (made during a few key times per season) provide important spatially integrated information to assess questions of spatial homogeneity in the source area footprints. This includes, for example, analyses and data presentation of physiological responses, including NEE, to diurnal environmental conditions, water stress, and other environmental controls and opens the way for additional analyses such as light response curves for the diversity of land surface types encountered along continuous flight lines from tens to hundreds of kilometers. Diurnal and seasonal patterns of NEE, H, λE, and energy balance across large inaccessible areas can be determined with repeated aircraft flights, and such an approach can alleviate the need for multiple towers at these, often remote, areas.

d. Rapidly evolving aircraft technologies

Aircraft-based flux measurement technologies continue to rapidly evolve. Since the certification of the SDSU Sky Arrow, there have been numerous improvements and advancements in the electronics within the MFP (see, e.g., Hall et al. 2006), including development of fast ultrasensitive temperature sensors (see, e.g., French et al. 2001) not requiring the complex corrections described here, implementation of advanced integrated inertial measurement unit (IMU) and GPS (IMU–GPS) electronics (see, e.g., Garman et al. 2006; Hall et al. 2006; Vellinga et al. 2010, 2013), as well as more durable and robust BAT probes and pressure spheres (see, e.g., Eckman et al. 2007; French et al. 2004). New wind tunnel tests (Dobosy et al. 2013; Garman et al. 2006) and calibration techniques and procedures (Garman et al. 2008, 2006; Vellinga et al. 2013) have improved the accuracy of wind vector calculations, while research into flux disaggregation methods (Hutjes et al. 2010; Kirby et al. 2008; Ogunjemiyo et al. 2003) and surface flux mapping techniques (e.g., Mauder et al. 2008) have improved associating surface fluxes to landscape elements in heterogeneous areas. Analysis strategies like the flight-path segmentation presented in Vellinga et al. (2010) allow for regional-scale estimates of heterogeneous terrain from aircraft-based fluxes based on landscape characteristics.

The miniaturization of electronics have also allowed for even smaller airborne platforms capable of flux measurements such as the microlight aircraft (see, e.g., Metzger et al. 2011, 2012) and even miniature unmanned aerial vehicles (UAVs; see, e.g., Spiess et al. 2007; Thomas et al. 2012; van den Kroonenberg et al. 2008). The latter potentially addressing the VFR flight limitations of manned aerial vehicles by being able to operate under marginal conditions, at night, or even

under severe conditions or in extremely remote locations considered either too dangerous or not feasible for manned aerial vehicles. Though the use of UAVs within the national airspace system is extremely limited at this time, aviation policies, procedures, and standards are being worked on by the various government agencies in order to accommodate and progress along with the rapidly evolving aircraft technologies.

5. Conclusions

Aircraft-based EC fluxes of CO_2, water vapor, energy, and momentum, as well as low-level remote sensing were successfully measured over the structurally and functionally complex coastal region of Magdalena Bay, Baja California Sur, Mexico. Our results demonstrate that the Sky Arrow aircraft was effective in characterizing and distinguishing land–atmosphere fluxes at spatial resolutions of 1 km across different heterogeneous landscapes. The increased sampling density of the aircraft provides fluxes at spatial resolutions that cannot be achieved by fixed location ground-based approaches alone. Aircraft-based EC techniques are a valuable tool to estimate regional-scale fluxes, particularly in areas that are logistically challenging or remote. Though aircraft can provide increased spatial sampling density, its temporal coverage is limited by flight rules and regulations, aircraft flight endurance, and weather conditions, as well as cost of deployment and operation. Therefore, aircraft-based measurements provide a strong compliment to tower-based EC and provide insight in the spatial distribution and patterns of fluxes. Combined with satellite-based information (e.g., MODIS) the aircraft approach yields measurements that can effectively be used to instruct, verify, and validate large-scale estimates from ecosystem process models as well as other satellite-derived data products and be instrumental in constraining the uncertainty in regional-scale fluxes.

Acknowledgments. This work was funded by grants from the National Science Foundation under OISE-0072140, DGE-0139378, and with funding for the initial development of the Sky Arrow under DBI-9604793. We acknowledge the support of W. T. Lawrence by the NOAA-funded Center of Excellence in Remote Sensing project, City College of New York. The authors thank the Centro de Investigaciones Biológicas del Noroeste for their Baja California Sur support and especially the invaluable help from L. Galvan, A. Michel, L. Miller, A. Mendieta, and J. L. Leon de la Luz. We are grateful to N. Kljun for providing us with the MATLAB code for her footprint model and ArcGIS assistance from J. Isles. We also thank TerraMetrics for providing the TruEarth 15-m-resolution satellite imagery. This paper has benefited by conversations with R. Hutjes, J. Elbers, R. Leuning, R. Desjardins, and S. Verma, as well as comments from H. Loescher, M. Mauder, D. Baldocchi, and several anonymous reviewers. The authors would like to dedicate this work to the late T. L. Crawford of the Field Research Division of the NOAA whose pioneering work and dedication to the use of small research aircraft has been instrumental in the development of the Sky Arrow.

APPENDIX

Aircraft Temperature Sensor Signal Attenuation and Correction

Inadequate dynamic frequency response of EC sensors results in some flux loss because of the high-frequency attenuation of the measured variances and covariances (Horst 1997, 2000; Massman 2000, 2001; Moore 1986). Typically, spectral corrections are based on analytical methods requiring the sensor time constant to be known (Moore 1986) or on determining the sensor attenuation transfer function assuming spectral and cospectral similarity with a nonattenuated variable (e.g., sonic temperature). In our case, none of these approaches were applicable to estimate flux loss and correct H since the theoretical time constant of temperature sensors is reported in still air and cannot be assumed valid in actual flight conditions. Since there is no nonattenuated reference variable, we adopted a fully data-driven approach based on isolating flight portions in different atmospheric stability conditions (i.e., neutral and unstable) and computed power spectra and retrieved the time constant by minimizing the mean square error, the match between observed and theoretical spectral shapes in the inertial subrange region (e.g., Kaimal and Finnigan 1994). Though the two aircraft microbead thermistors (Tp_1 and Tp_2) were the same sensor type, they were located in two different physical locations within the BAT probe hemisphere and therefore aspirated differently while in flight. The signal attenuation was expected to be different as a result of Tp_1 being in the center and aspirating at $5\,m\,s^{-1}$, while the Tp_2 sensor within the fast flow port aspirated at true airspeeds. Power spectra were analyzed to determine the signal attenuation of each sensor.

Normalized power spectra were first created by identifying two homogeneous surfaces within the study region, ocean and desert sand. During the flights the atmospheric stability over the ocean was always in near neutral conditions, while over the desert sand surface it was in unstable conditions. A total of 32 transects was available over the ocean and 30 over the desert, with

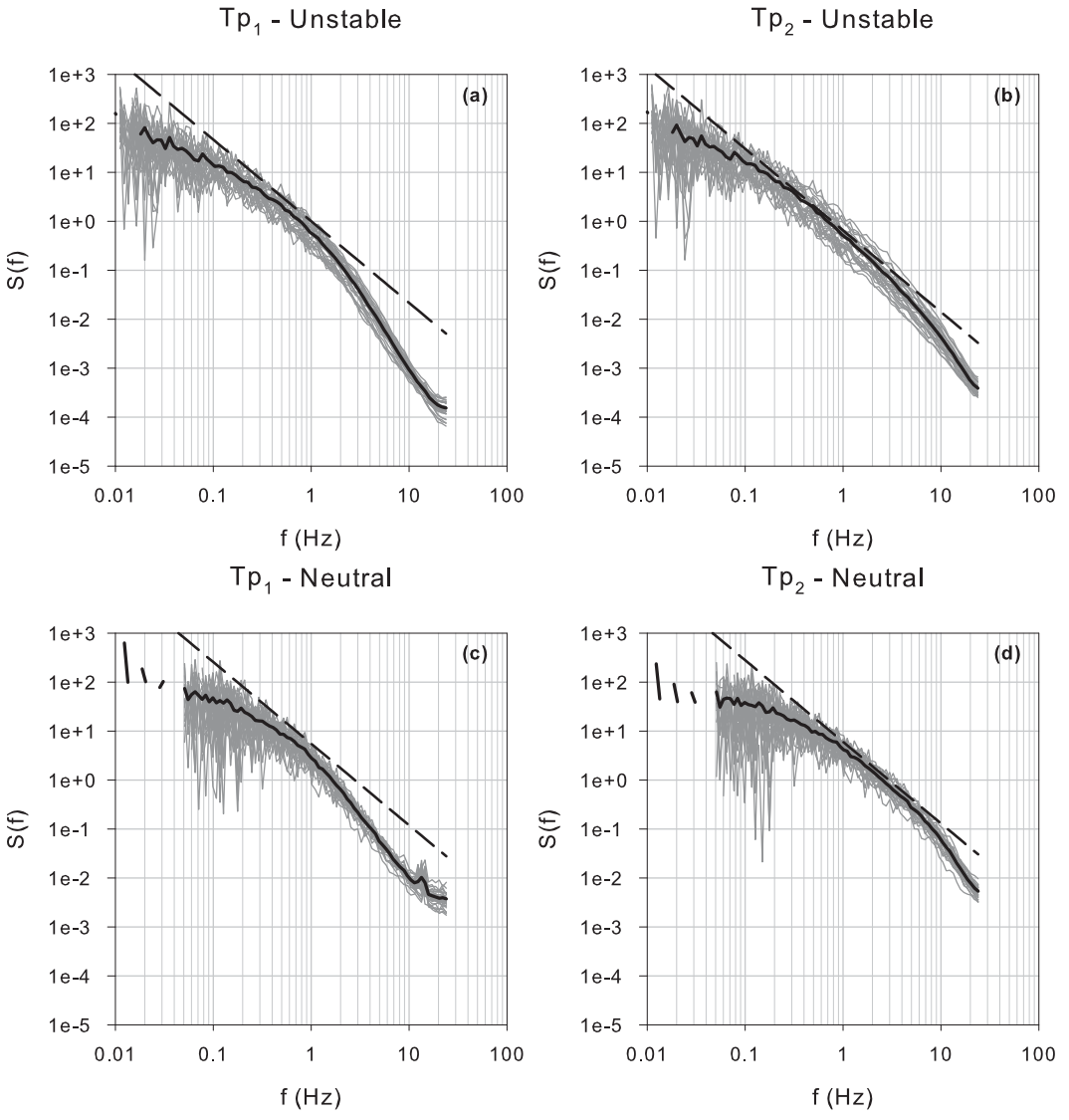

FIG. A1. Normalized power spectra for Tp_1 and Tp_2 sensors in unstable (desert transect) and neutral (sea transect) conditions. Gray lines are spectra for single individual transects, the solid black line is the average spectra, and the dashed line is the $-5/3$ slope power law.

four exclusions over each surface due to sporadic low-frequency contributions. Power spectra highlighted a larger attenuation in the Tp_1 sensor, particularly in neutral conditions where smaller eddies (i.e., higher frequencies) are relatively more important (Fig. A1). Therefore, the less attenuated Tp_2 sensor was selected for calculations of H.

A first-order gain transfer function $H_c(f)$ describes the dynamic frequency response of the aircraft temperature sensors, given by

$$H_c(f) = \frac{1}{1 + (2\pi f \tau_c)}, \tag{A1}$$

where τ_c is the time constant and f is the sampling frequency. The observed attenuated power spectra $S(f)$ can therefore be expressed as

$$S(f) = \frac{S_0(f)}{H_c(f)}, \tag{A2}$$

where $S_0(f)$ is the real power spectra and $H_c(f)$ is the transfer function from Eq. (A1).

The $-5/3$ power law represents the theoretical spectral shape within the inertial subrange region (Kolmogorov 1941; Obukhov 1941). To constrain the fit in the inertial subrange, we used the region between 1 and 10 Hz,

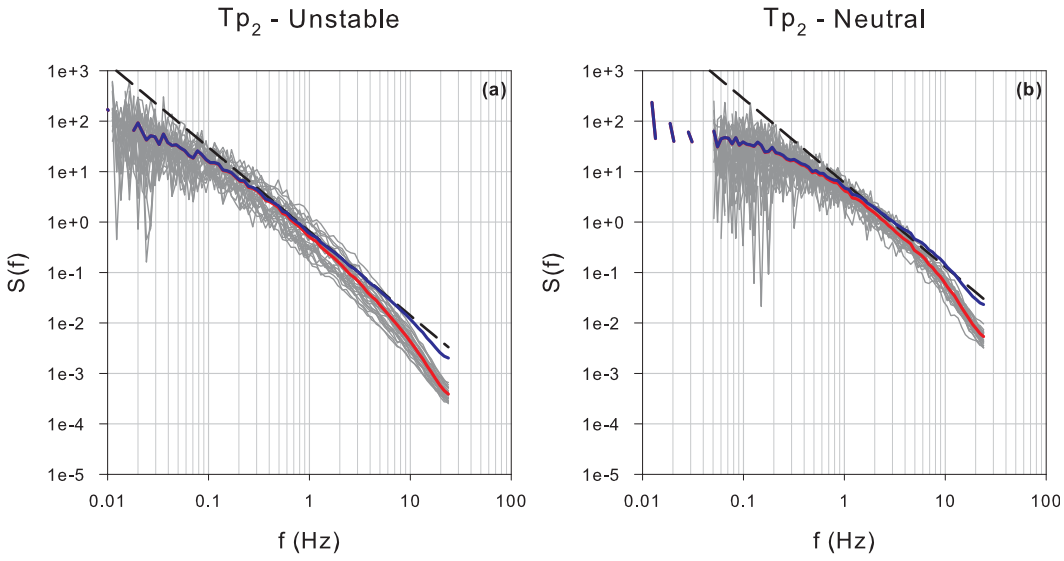

FIG. A2. Normalized observed and corrected power spectra for the Tp_2 sensor in (a) unstable (desert transect) and (b) neutral (sea transect) conditions. Gray lines are spectra for single individual transects, the solid red line is the average spectra, the solid blue line is the corrected spectra, and the dashed line is the $-5/3$ slope power law.

excluding higher frequencies because of possible aliasing and assumed a null attenuation for signals <1 Hz. The τ_c was estimated as the best fit between corrected and theoretical spectra at 0.022 and 0.028 s for neutral and unstable conditions, respectively. The average value of 0.025 s was used for the subsequent data processing. Figure A2 shows the observed and corrected power spectra corresponding to the neutral (τ_c = 0.022 s) and unstable (τ_c = 0.028 s) conditions, and Fig. A3 shows the uncorrected and corrected (τ_c = 0.025 s) Tp_2 power spectra for a single flight.

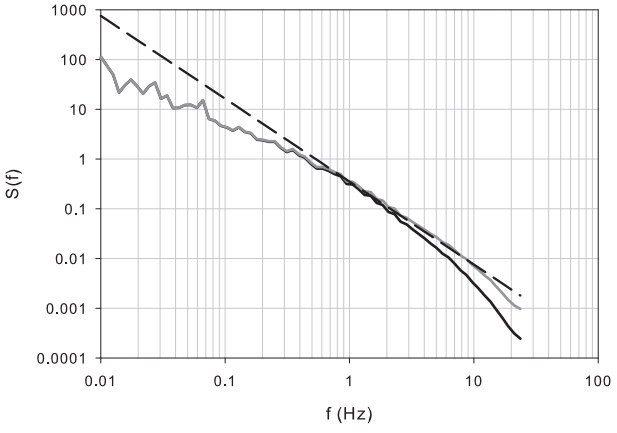

FIG. A3. Normalized average raw power spectra (solid black line) and time-response corrected (τ_c = 0.025 s) spectra (solid gray line) for Tp_2 for a single flight on 27 Jul 2004. The dashed line is the $-5/3$ slope power law.

REFERENCES

Alongi, D. M., 2002: Present state and future of the world's mangrove forests. *Environ. Conserv.,* **29,** 331–349, doi:10.1017/s0376892902000231.

——, 2009: *The Energetics of Mangrove Forests.* Springer, 216 pp.

Alvarez-Borrego, S., L. A. Galindo-Bect, and A. Chee-Barragan, 1975: Características hidroquímicas de Bahía Magdalena, B.C.S. *Cienc. Mar.,* **2,** 94–110.

Andreas, E. L, 1981: The effects of volume averaging on spectra measured with a Lyman-alpha hygrometer. *J. Appl. Meteor.,* **20,** 467–475.

Asher, W. E., L. M. Karle, B. J. Higgins, P. J. Farley, E. C. Monahan, and I. S. Leifer, 1996: The influence of bubble plumes on air-seawater gas transfer velocities. *J. Geophys. Res.,* **101** (C5), 12 027–12 041.

Aubinet, M., and Coauthors, 2000: Estimates of the annual net carbon and water exchange of forests: The EUROFLUX methodology. *Advances in Ecological Research,* A. H. Fitter and D. G. Raffaelli, Eds., Academic Press, 113–175.

Baldocchi, D. D., B. B. Hicks, and T. P. Meyers, 1988: Measuring biosphere-atmosphere exchanges of biologically related gases with micrometeorological methods. *Ecology,* **69,** 1331–1340.

——, and Coauthors, 2001: FLUXNET: A new tool to study the temporal and spatial variability of ecosystem-scale carbon dioxide, water vapor, and energy flux densities. *Bull. Amer. Meteor. Soc.,* **82,** 2415–2434.

Barr, J. G., V. Engel, J. D. Fuentes, J. C. Zieman, T. L. O'Halloran, T. J. Smith, and G. H. Anderson, 2010: Controls on mangrove forest-atmosphere carbon dioxide exchanges in western Everglades National Park. *J. Geophys. Res.,* **115,** G02020, doi:10.1029/2009jg001186.

Bell, T. W., O. Menzer, E. Troyo-Diéquez, and W. C. Oechel, 2012: Carbon dioxide exchange over multiple temporal scales in an arid shrub ecosystem near La Paz, Baja California Sur, Mexico. *Global Change Biol.,* **18,** 2570–2582, doi:10.1111/j.1365-2486.2012.02720.x.

Beringer, J., L. B. Hutley, J. M. Hacker, B. Neininger, and K. T. Paw U, 2011a: Patterns and processes of carbon, water and energy cycles across northern Australian landscapes: From point to region. *Agric. For. Meteor.,* **151,** 1409–1416, doi:10.1016/j.agrformet.2011.05.003.

——, and Coauthors, 2011b: SPECIAL—Savanna Patterns of Energy and Carbon Integrated Across the Landscape. *Bull. Amer. Meteor. Soc.,* **92,** 1467–1485.

Biehl, L., and D. Landgrebe, 2002: MultiSpec—A tool for multispectral-hyperspectral image data analysis. *Comput. Geosci.,* **28,** 1153–1159.

Bizzarro, J. J., 2008: A review of the physical and biological characteristics of the Bahia Magdalena lagoon complex (Baja California Sur, Mexico). *Bull. South. Calif. Acad. Sci.,* **107,** 1–24.

Bögel, W., and R. Baumann, 1991: Test and calibration of the DLR Falcon wind measuring system by maneuvers. *J. Atmos. Oceanic Technol.,* **8,** 5–18.

Borges, A. V., S. Djenidi, G. Lacroix, J. Theate, B. Delille, and M. Frankignoulle, 2003: Atmospheric CO_2 flux from mangrove surrounding waters. *Geophys. Res. Lett.,* **30,** 1558, doi:10.1029/2003gl017143.

Bouillon, S., and Coauthors, 2008: Mangrove production and carbon sinks: A revision of global budget estimates. *Global Biogeochem. Cycles,* **22,** GB2013, doi:10.1029/2007gb003052.

Box, E. O., B. N. Holben, and V. Kalb, 1989: Accuracy of the AVHRR vegetation index as a predictor of biomass, primary productivity and net CO_2 flux. *Vegetatio,* **80,** 71–89.

Broecker, W. S., and T. Takahashi, 1966: Calcium carbonate precipitation on the Bahama Banks. *J. Geophys. Res.,* **71,** 1575–1602.

Brooks, S., T. L. Crawford, R. T. McMillen, and E. Dumas, 1996: Airborne measurements of mass, momentum, and energy fluxes, Arctic Landscape Flux Survey (ALFS)—1994, 1995. NOAA Tech. Memo. ARL/ATDD-216, 41 pp.

Brown, E. N., C. A. Friehe, and D. H. Lenschow, 1983: The use of pressure fluctuations on the nose of an aircraft for measuring air motion. *J. Climate Appl. Meteor.,* **22,** 171–180.

Cai, W.-J., M. Dai, and Y. Wang, 2006: Air-sea exchange of carbon dioxide in ocean margins: A province-based synthesis. *Geophys. Res. Lett.,* **33,** L12603, doi:10.1029/2006gl026219.

Chavez, R. S., 2006: El papel de los manglares en la producción de las comunidades acuáticas de Bahía Magdalena, B.C.S. (The role of mangroves in the aquatic community production of Magdalena Bay, B.C.S.). Tesis Doctoral, Centro Interdisciplinario de Ciencias Marinas IPN, 127 pp.

Cliffton, K., D. O. Cornejo, and R. S. Felger, 1995: Sea turtles of the Pacific coast of Mexico. *Biology and Conservation of Sea Turtles,* K. A. Bjorndal, Ed., Smithsonian Institution Press, 199–209.

Cohen, W. B., T. K. Maiersperger, Z. Yang, S. T. Gower, D. P. Turner, W. D. Ritts, M. Berterretche, and S. W. Running, 2003: Comparisons of land cover and LAI estimates derived from ETM+ and MODIS for four sites in North America: A quality assessment of 2000/2001 provisional MODIS products. *Remote Sens. Environ.,* **88,** 233–255, doi:10.1016/j.rse.2003.06.006.

Costanza, R., and Coauthors, 1997: The value of the world's ecosystem services and natural capital. *Nature,* **387,** 253–260.

Crawford, T. L., and R. J. Dobosy, 1992: A sensitive fast-response probe to measure turbulence and heat flux from any airplane. *Bound.-Layer Meteor.,* **59,** 257–278, doi:10.1007/BF00119816.

——, R. T. McMillen, and R. J. Dobosy, 1990: Development of a ''generic'' mobile flux platform with demonstration on a small airplane. NOAA Tech. Memo. ERL ARL-184, 81 pp.

——, ——, ——, and I. MacPherson, 1993a: Correcting airborne flux measurements for aircraft speed variation. *Bound.-Layer Meteor.,* **66,** 237–245, doi:10.1007/BF00705476.

——, ——, T. P. Meyers, and B. B. Hicks, 1993b: Spatial and temporal variability of heat, water vapor, carbon dioxide, and momentum air-sea exchange in a coastal environment. *J. Geophys. Res.,* **98** (D7), 12 869–12 880.

——, R. J. Dobosy, and E. J. Dumas, 1996a: Aircraft wind measurement considering lift-induced upwash. *Bound.-Layer Meteor.,* **80,** 79–94, doi:10.1007/BF00119012.

——, ——, R. T. McMillen, C. A. Vogel, and B. B. Hicks, 1996b: Air-surface exchange measurement in heterogeneous regions: Extending tower observations with spatial structure observed from small aircraft. *Global Change Biol.,* **2,** 275–285.

Desai, A. R., and Coauthors, 2008: Influence of vegetation and seasonal forcing on carbon dioxide fluxes across the upper Midwest, USA: Implications for regional scaling. *Agric. For. Meteor.,* **148,** 288–308, doi:10.1016/j.agrformet.2007.08.001.

——, B. R. Helliker, P. R. Moorcroft, A. E. Andrews, and J. A. Berry, 2010: Climatic controls of interannual variability in regional carbon fluxes from top-down and bottom-up perspectives. *J. Geophys. Res.,* **115,** G02011, doi:10.1029/2009JG001122.

Desjardins, R. L., J. I. Macpherson, P. H. Schuepp, and F. Karanja, 1989: An evaluation of aircraft flux measurements of CO_2, water vapor and sensible heat. *Bound.-Layer Meteor.,* **47,** 55–69, doi:10.1007/BF00122322.

——, R. L. Hart, J. I. MacPherson, P. H. Schuepp, and S. B. Verma, 1992: Aircraft- and tower-based fluxes of carbon dioxide, latent, and sensible heat. *J. Geophys. Res.,* **97** (D17), 18 477–18 485.

——, and Coauthors, 1997: Scaling up flux measurements for the boreal forest using aircraft-tower combinations. *J. Geophys. Res.,* **102** (D24), 29 125–29 133.

Dobosy, R., and Coauthors, 2013: Calibration and quality assurance of an airborne turbulence probe in an aeronautical wind tunnel. *J. Atmos. Oceanic Technol.,* **30,** 182–196.

Dolman, A. J., and Coauthors, 2006: The CarboEurope Regional Experiment Strategy. *Bull. Amer. Meteor. Soc.,* **87,** 1367–1379.

——, C. Gerbig, J. Noilhan, C. Sarrat, and F. Miglietta, 2009: Detecting regional variability in sources and sinks of carbon dioxide: A synthesis. *Biogeosciences,* **6,** 1015–1026.

Duke, N. C., and Coauthors, 2007: A world without mangroves? *Science,* **317,** 41–42.

Dumas, E. J., S. B. Brooks, and J. Verfaillie, 2001: Development and testing of a Sky Arrow 650 ERA for atmospheric research. Preprints, *11th Symp. on Meteorological Observations and Instrumentation,* Albuquerque, NM, Amer. Meteor. Soc., 5.8. [Available online at https://ams.confex.com/ams/annual2001/techprogram/paper_18395.htm.]

Eckman, R. M., cited 2012: Computation of flow angles and dynamic pressure on BAT probe. NOAA/ARL Field Research Division. [Available online at http://www.noaa.inel.gov/Personnel/Eckman/docs/flowangles.pdf.]

——, T. L. Crawford, E. J. Dumas, and K. R. Birdwell, 1999: Airborne meteorological measurements collected during the Model Validation Program (MVP) field experiments at Cape Canaveral, Florida. NOAA Tech. Memo. ARL/ATDD-233, 61 pp.

——, R. J. Dobosy, D. L. Auble, T. W. Strong, and T. L. Crawford, 2007: A pressure-sphere anemometer for measuring turbulence and fluxes in hurricanes. *J. Atmos. Oceanic Technol.,* **24,** 994–1007.

Falge, E., and Coauthors, 2001: Gap filling strategies for defensible annual sums of net ecosystem exchange. *Agric. For. Meteor.,* **107,** 43–69.

Farmer, D. M., C. L. McNeil, and B. D. Johnson, 1993: Evidence of the importance of bubbles in increasing air–sea gas flux. *Nature,* **361,** 620–623.

Foken, T., 2006: 50 years of the Monin–Obukhov similarity theory. *Bound.-Layer Meteor.,* **119,** 431–447, doi:10.1007/s10546-006-9048-6.

French, J. R., T. L. Crawford, R. C. Johnson, and O. R. Cote, 2001: A high-resolution temperature probe for airborne measurements. Preprints, *11th Symp. on Meteorological Observations and Instrumentation,* Albuquerque, NM, Amer. Meteor. Soc., 139–141.

——, R. Johnson, S. Beard, and T. Crawford, 2004: Modification of an airborne gust probe for hurricane boundary layer research. Preprints, *26th Conf. on Hurricanes and Tropical Meteorology,* Miami, FL, Amer. Meteor. Soc., P1.42. [Available online at https://ams.confex.com/ams/26HURR/webprogram/Paper75769.html.]

Friehe, C. A., and Coauthors, 1991: Air-sea fluxes and surface-layer turbulence around a sea-surface temperature front. *J. Geophys. Res.,* **96** (C5), 8593–8609.

Garman, K. E., and Coauthors, 2006: An airborne and wind tunnel evaluation of a wind turbulence measurement system for aircraft-based flux measurements. *J. Atmos. Oceanic Technol.,* **23,** 1696–1708.

——, P. Wyss, M. Carlsen, J. R. Zimmerman, B. H. Stirm, T. Q. Carney, R. Santini, and P. B. Shepson, 2008: The contribution of variability of lift-induced upwash to the uncertainty in vertical winds determined from an aircraft platform. *Bound.-Layer Meteor.,* **126,** 461–476, doi:10.1007/s10546-007-9237-y.

Gioli, B., and Coauthors, 2004: Comparison between tower and aircraft-based eddy covariance fluxes in five European regions. *Agric. For. Meteor.,* **127,** 1–16, doi:10.1016/j.agrformet.2004.08.004.

——, F. Miglietta, F. P. Vaccari, A. Zaldei, and B. De Martino, 2006: The Sky Arrow ERA, an innovative airborne platform to monitor mass, momentum and energy exchange of ecosystems. *Ann. Geophys.,* **49,** 109–116.

Glenn, E. P., P. L. Nagler, R. C. Brusca, and O. Hinojosa-Huerta, 2006: Coastal wetlands of the northern Gulf of California: Inventory and conservation status. *Aquat. Conserv.-Mar. Freshwater Ecosyst.,* **16,** 5–28, doi:10.1002/aqc.681.

Goulden, M. L., J. W. Munger, S.-M. Fan, B. C. Daube, and S. C. Wofsy, 1996: Measurements of carbon sequestration by long-term eddy covariance: Methods and a critical evaluation of accuracy. *Global Change Biol.,* **2,** 169–182, doi:10.1111/j.1365-2486.1996.tb00070.x.

Goward, S. N., B. Markham, D. G. Dye, W. Dulaney, and J. L. Yang, 1991: Normalized difference vegetation index measurements from the Advanced Very High Resolution Radiometer. *Remote Sens. Environ.,* **35,** 257–277.

Gu, L. H., and Coauthors, 2005: Objective threshold determination for nighttime eddy flux filtering. *Agric. For. Meteor.,* **128,** 179–197, doi:10.1016/j.agrformet.2004.11.006.

Gurvich, A. S., 1962: The pulsation spectra of the vertical component of wind velocity and their relations to the micrometeorological conditions. *Tr. Akad. Nauk SSSR Inst. Fiz. Atmos.,* **4,** 101–136.

Hacker, J. M., and T. L. Crawford, 1999: The BAT Probe: The ultimate tool to measure turbulence from any kind of aircraft (or sailplane). *Tech. Soaring,* **23,** 43–46.

Hales, B., T. Takahashi, and L. Bandstra, 2005: Atmospheric CO_2 uptake by a coastal upwelling system. *Global Biogeochem. Cycles,* **19,** GB1009, doi:10.1029/2004GB002295.

Hall, P. G., E. J. Dumas, and D. L. Senn, 2006: NOAA ARL mobile flux platform instrumentation integration on University of Alabama Sky Arrow environmental aircraft. NOAA Tech. Memo. ERL ARL-257, 51 pp.

Hastings, J. R., and R. M. Turner, 1965: Seasonal precipitation regimes in Baja California, Mexico. *Geogr. Ann.,* **47A,** 204–223.

Hastings, S. J., W. C. Oechel, and A. Muhlia-Melo, 2005: Diurnal, seasonal and annual variation in the net ecosystem CO_2 exchange of a desert shrub community (sarcocaulescent) in Baja California, Mexico. *Global Change Biol.,* **11,** 927–939.

Heinsch, F. A., and Coauthors, 2006: Evaluation of remote sensing based terrestrial productivity from MODIS using regional tower eddy flux network observations. *IEEE Trans. Geosci. Remote Sens.,* **44,** 1908–1925, doi:10.1109/TGRS.2005.853936.

Hinkel, K. M., F. Paetzold, F. E. Nelson, and J. G. Bockheim, 2001: Patterns of soil temperature and moisture in the active layer and upper permafrost at Barrow, Alaska: 1993–1999. *Global Planet. Change,* **29,** 293–309, doi:10.1016/s0921-8181(01)00096-0.

Horst, T. W., 1997: A simple formula for attenuation of eddy fluxes measured with first-order-response scalar sensors. *Bound.-Layer Meteor.,* **82,** 219–233.

——, 2000: On frequency response corrections for eddy covariance flux measurements. *Bound.-Layer Meteor.,* **94,** 517–520, doi:10.1023/a:1002427517744.

Hutjes, R. W. A., O. S. Vellinga, B. Gioli, and F. Miglietta, 2010: Dis-aggregation of airborne flux measurements using footprint analysis. *Agric. For. Meteor.,* **150,** 966–983, doi:10.1016/j.agrformet.2010.03.004.

Huxman, T. E., and Coauthors, 2004: Precipitation pulses and carbon fluxes in semiarid and arid ecosystems. *Oecologia,* **141,** 254–268, doi:10.1007/s00442-004-1682-4.

Ikawa, H, 2012: Air–sea CO_2 exchange of the coastal marine zone. Ph.D. dissertation, San Diego State University, 207 pp.

Isaac, P. R., J. McAneney, R. Leuning, and J. M. Hacker, 2004: Comparison of aircraft and ground-based flux measurements during OASIS95. *Bound.-Layer Meteor.,* **110,** 39–67, doi:10.1023/A:1026002301152.

Kaimal, J. C., and J. J. Finnigan, 1994: *Atmospheric Boundary Layer Flows: Their Structure and Measurement.* Oxford University Press, 289 pp.

——, J. C. Wyngaard, Y. Izumi, and O. R. Coté, 1972: Spectral characteristics of surface-layer turbulence. *Quart. J. Roy. Meteor. Soc.,* **98,** 563–589, doi:10.1002/qj.49709841707.

——, S. F. Clifford, and R. J. Lataitis, 1989: Effect of finite sampling on atmospheric spectra. *Bound.-Layer Meteor.,* **47,** 337–347.

Kalogiros, J. A., and Q. Wang, 2002a: Calibration of a radome-differential GPS system on a Twin Otter research aircraft for turbulence measurements. *J. Atmos. Oceanic Technol.,* **19,** 159–171.

——, and ——, 2002b: Aerodynamic effects on wind turbulence measurements with research aircraft. *J. Atmos. Oceanic Technol.,* **19,** 1567–1576.

Kelly, R. D., E. A. Smith, and J. I. MacPherson, 1992: A comparison of surface sensible and latent heat fluxes from aircraft and surface measurements in FIFE 1987. *J. Geophys. Res.,* **97** (D17), 18 445–18 453.

Khelif, D., S. P. Burns, and C. A. Friehe, 1999: Improved wind measurements on research aircraft. *J. Atmos. Oceanic Technol.,* **16,** 860–875.

Kirby, S., R. Dobosy, D. Williamson, and E. Dumas, 2008: An aircraft-based data analysis method for discerning individual fluxes in a heterogeneous agricultural landscape. *Agric. For. Meteor.,* **148,** 481–489, doi:10.1016/j.agrformet.2007.10.011.

Kljun, N., M. W. Rotach, and H. P. Schmid, 2002: A three-dimensional backward Lagrangian footprint model for a wide range of boundary-layer stratifications. *Bound.-Layer Meteor.,* **103,** 205–226.

——, P. Calanca, M. Rotach, and H. Schmid, 2004: A simple parameterisation for flux footprint predictions. *Bound.-Layer Meteor.,* **112,** 503–523, doi:10.1023/b:boun.0000030653.71031.96.

Knapp, A. K., and M. D. Smith, 2001: Variation among biomes in temporal dynamics of aboveground primary production. *Science,* **291,** 481–484.

Kolmogorov, A. N., 1941: Energy dissipation in locally isotropic turbulence. *Dokl. Akad. Nauk SSSR,* **32,** 19–21.

Kristensen, L., and N. O. Jensen, 1979: Lateral coherence in isotropic turbulence and in the natural wind. *Bound.-Layer Meteor.,* **17,** 353–373, doi:10.1007/bf00117924.

——, and D. R. Fitzjarrald, 1984: The effect of line averaging on scalar flux measurements with a sonic anemometer near the surface. *J. Atmos. Oceanic Technol.,* **1,** 138–146.

Leclerc, M. Y., and G. W. Thurtell, 1990: Footprint prediction of scalar fluxes using a Markovian analysis. *Bound.-Layer Meteor.,* **52,** 247–258.

Leise, J. A., and J. M. Masters, 1993: Wind measurement from aircraft. *Aircraft Operations Center,* National Oceanic and Atmospheric Administration, 168 pp.

LeMone, M. A., R. L. Grossman, F. Chen, K. Ikeda, and D. Yates, 2003: Choosing the averaging interval for comparison of observed and modeled fluxes along aircraft transects over a heterogeneous surface. *J. Hydrometeor.,* **4,** 179–195.

Lenschow, D. H., 1986: Aircraft measurements in the boundary layer. *Probing the Atmospheric Boundary Layer,* D. H. Lenschow, Ed., Amer. Meteor. Soc., 39–55.

——, J. Mann, and L. Kristensen, 1994: How long is long enough when measuring fluxes and other turbulence statistics? *J. Atmos. Oceanic Technol.,* **11,** 661–673.

——, V. Savic-Jovcic, and B. Stevens, 2007: Divergence and vorticity from aircraft air motion measurements. *J. Atmos. Oceanic Technol.,* **24,** 2062–2072.

Loescher, H. W., B. E. Law, L. Mahrt, D. Y. Hollinger, J. Campbell, and S. C. Wofsy, 2006a: Uncertainties in, and interpretation of, carbon flux estimates using the eddy covariance technique. *J. Geophys. Res.,* **111,** D21S90, doi:10.1029/2005JD006932.

——, G. Starr, T. A. Martin, M. Binford, and H. L. Gholz, 2006b: The effect of local atmospheric circulations on daytime carbon dioxide flux measurements over a *Pinus elliottii* canopy. *J. Appl. Meteor. Climatol.,* **45,** 1127–1140.

Lumley, J. L., and H. A. Panofsky, 1964: *The Structure of Atmospheric Turbulence.* Vol. 12. Interscience, 239 pp.

Mahrt, L., 1998: Flux sampling errors for aircraft and towers. *J. Atmos. Oceanic Technol.,* **15,** 416–429.

Mann, J., and D. H. Lenschow, 1994: Errors in airborne flux measurements. *J. Geophys. Res.,* **99** (D7), 14 519–14 526.

Marshall, J. D., J. M. Blair, D. P. C. Peters, G. Okin, A. Rango, and M. Williams, 2008: Predicting and understanding ecosystem responses to climate change at continental scales. *Front. Ecol. Environ,* **6,** 273–280, doi:10.1890/070165.

Massman, W. J., 2000: A simple method for estimating frequency response corrections for eddy covariance systems. *Agric. For. Meteor.,* **104,** 185–198, doi:10.1016/s0168-1923(00)00164-7.

——, 2001: Reply to comment by Rannik on ''A simple method for estimating frequency response corrections for eddy covariance systems.'' *Agric. For. Meteor.,* **107,** 247–251, doi:10.1016/s0168-1923(00)00237-9.

Mauder, M., R. L. Desjardins, and I. MacPherson, 2008: Creating surface flux maps from airborne measurements: Application to the Mackenzie Area GEWEX Study MAGS 1999. *Bound.-Layer Meteor.,* **129,** 431–450, doi:10.1007/s10546-008-9326-6.

McMillen, R. T., 1986: A BASIC program for eddy correlation in nonsimple terrain. NOAA Tech. Memo. ERL ARL-147, 32 pp.

——, 1988: An eddy correlation technique with extended applicability to non-simple terrain. *Bound.-Layer Meteor.,* **43,** 231–245.

McNeil, C., and E. D'Asaro, 2007: Parameterization of air-sea gas fluxes at extreme wind speeds. *J. Mar. Syst.,* **66,** 110–121, doi:10.1016/j.jmarsys.2006.05.013.

Metzger, S., W. Junkermann, K. Butterbach-Bahl, H. P. Schmid, and T. Foken, 2011: Corrigendum to ''Measuring the 3-D wind vector with a weight-shift microlight aircraft'' published in Atmos. Meas. Tech., 4, 1421–1444, 2011. *Atmos. Meas. Tech.,* **4,** 1515–1539, doi:10.5194/amt-4-1515-2011.

——, ——, M. Mauder, F. Beyrich, K. Butterbach-Bahl, H. P. Schmid, and T. Foken, 2012: Eddy-covariance flux measurements with a weight-shift microlight aircraft. *Atmos. Meas. Tech.,* **5,** 1699–1717, doi:10.5194/amt-5-1699-2012.

Monin, A. S., and A. M. Obukhov, 1954: Osnovnye zakonomernosti turbulentnogo peremeshivanija v prizemnom sloe atmosfery (Basic laws of turbulent mixing in the surface layer of the atmosphere). *Tr. Geofiz. Insit. Akad. Nauk SSSR,* **24,** 163–187.

Moore, C. J., 1986: Frequency-response corrections for eddy-correlation systems. *Bound.-Layer Meteor.,* **37,** 17–35.

Myneni, R. B., R. R. Nemani, and S. W. Running, 1997: Estimation of global leaf area index and absorbed PAR using radiative transfer models. *IEEE Trans. Geosci. Remote Sens.,* **35,** 1380–1393.

Nagelkerken, I., and Coauthors, 2008: The habitat function of mangroves for terrestrial and marine fauna: A review. *Aquat. Bot.,* **89,** 155–185.

National Research Council, 2001: *Grand Challenges in Environmental Sciences.* National Academies Press, 106 pp.

——, 2003: *NEON: Addressing the Nation's Environmental Challenges.* National Academies Press, 132 pp.

Obukhov, A. M., 1941: Energy distribution in the spectrum of a turbulent flow. *Izventiya AN SSR, Ser. Geogr. Geofiz,* 453–466.

——, 1946: Turbulentnost v temperaturnoj- neodnorodnoj atmosfere (Turbulence in an atmosphere with a non-uniform temperature). *Tr. Instit. Theoreticheskio Geofiz. AN SSSR,* **1,** 95–115.

——, 1971: Turbulence in an atmosphere with a non-uniform temperature. *Bound.-Layer Meteor.,* **2,** 7–29, doi:10.1007/bf00718085.

Oechel, W. C., G. L. Vourlitis, S. Brooks, T. L. Crawford, and E. Dumas, 1998: Intercomparison among chamber, tower, and aircraft net CO_2 and energy fluxes measured during the Arctic System Science Land-Atmosphere-Ice Interactions (ARCSS-LAII) flux study. *J. Geophys. Res.,* **103** (D22), 28 993–29 003.

——, and Coauthors, 2000: A scaling approach for quantifying the net CO_2 flux of the Kuparuk River basin, Alaska. *Global Change Biol.,* **6,** 160–173, doi:10.1046/j.1365-2486.2000.06018.x.

Ogunjemiyo, S. O., P. H. Schuepp, J. I. MacPherson, and R. L. Desjardins, 1997: Analysis of flux maps versus surface

characteristics from Twin Otter grid flights in BOREAS 1994. *J. Geophys. Res.,* **102** (D24), 29 135–29 145.

——, S. K. Kaharabata, P. H. Schuepp, I. J. MacPherson, R. L. Desjardins, and D. A. Roberts, 2003: Methods of estimating CO_2, latent heat and sensible heat fluxes from estimates of land cover fractions in the flux footprint. *Agric. For. Meteor.,* **117,** 125–144, doi:10.1016/s0168-1923(03)00061-3.

Oncley, S. P., C. A. Friehe, J. C. Larue, J. A. Businger, E. C. Itsweire, and S. S. Chang, 1996: Surface-layer fluxes, profiles, and turbulence measurements over uniform terrain under near-neutral conditions. *J. Atmos. Sci.,* **53,** 1029–1044.

Osborne, P. L., 2000: *Tropical Ecosystems and Ecological Concepts.* Cambridge University Press, 464 pp.

Paez-Osuna, F., A. Gracia, F. Flores-Verdugo, L. P. Lyle-Fritch, R. Alonso-Rodriguez, A. Roque, and A. C. Ruiz-Fernandez, 2003: Shrimp aquaculture development and the environment in the Gulf of California ecoregion. *Mar. Pollut. Bull.,* **46,** 806–815, doi:10.1016/s0025-326x(03)00107-3.

Paw U, K. T., D. D. Baldocchi, T. P. Meyers, and K. B. Wilson, 2000: Correction of eddy-covariance measurements incorporating both advective effects and density fluxes. *Bound.-Layer Meteor.,* **97,** 487–511, doi:10.1023/A:1002786702909.

Peters, D. P. C., P. M. Groffman, K. J. Nadelhoffer, N. B. Grimm, S. L. Coffins, W. K. Michener, and M. A. Huston, 2008: Living in an increasingly connected world: A framework for continental-scale environmental science. *Front. Ecol. Environ.,* **6,** 229–237, doi:10.1890/070098.

Reichstein, M., and Coauthors, 2005: On the separation of net ecosystem exchange into assimilation and ecosystem respiration: Review and improved algorithm. *Global Change Biol.,* **11,** 1424–1439, doi:10.1111/j.1365-2486.2005.001002.x.

Reid, W. V., and Coauthors, 2006: Nature: The many benefits of ecosystem services. *Nature,* **443,** 749–749, doi:10.1038/443749a.

Rew, R., G. Davis, S. Emmerson, and H. Davies, 1997: *NetCDF User's Guide for C: An Access Interface for Self-Describing, Portable Data, Version 3.* University Center for Atmospheric Research, Unidata Program Center, 129 pp.

Reynolds, J. F., P. R. Kemp, K. Ogle, and R. J. Fernández, 2004: Modifying the 'pulse–reserve' paradigm for deserts of North America: Precipitation pulses, soil water, and plant responses. *Oecologia,* **141,** 194–210, doi:10.1007/s00442-004-1524-4.

Riedel, S. M., H. E. Epstein, D. A. Walker, D. L. Richardson, M. P. Calef, E. Edwards, and A. Moody, 2005: Spatial and temporal heterogeneity of vegetation properties among four tundra plant communities at Ivotuk, Alaska, U.S.A. *Arct. Antarct. Alp. Res.,* **37,** 25–33, doi:10.1657/1523-0430(2005)037[0025:sathov]2.0.co;2.

Sasai, T., K. Ichii, Y. Yamaguchi, and R. Nemani, 2005: Simulating terrestrial carbon fluxes using the new biosphere model ''biosphere model integrating eco-physiological and mechanistic approaches using satellite data'' (BEAMS). *J. Geophys. Res.,* **110,** G02014, doi:10.1029/2005JG000045.

——, K. Okamoto, T. Hiyama, and Y. Yamaguchi, 2007: Comparing terrestrial carbon fluxes from the scale of a flux tower to the global scale. *Ecol. Modell.,* **208,** 135–144, doi:10.1016/j.ecolmodel.2007.05.014.

Schimel, D., and Coauthors, 2011: NEON 2011 Science Strategy: Enabling continental-scale ecological forecasting. NEON Rep., NEON Inc., Boulder, CO, 55 pp. [Available online at www.neoninc.org/science/sciencestrategy.]

Schmid, H. P., 2002: Footprint modeling for vegetation atmosphere exchange studies: A review and perspective. *Agric. For. Meteor.,* **113,** 159–183, doi:10.1016/S0168-1923(02)00107-7.

Schuepp, P. H., M. Y. Leclerc, J. I. MacPherson, and R. L. Desjardins, 1990: Footprint prediction of scalar fluxes from analytical solutions of the diffusion equation. *Bound.-Layer Meteor.,* **50,** 355–373, doi:10.1007/bf00120530.

Scott, S. G., T. P. Bui, K. R. Chan, and S. W. Bowen, 1990: The meteorological measurement system on the NASA ER-2 aircraft. *J. Atmos. Oceanic Technol.,* **7,** 525–540.

Sellers, P. J., 1985: Canopy reflectance, photosynthesis and transpiration. *Int. J. Remote Sens.,* **6,** 1335–1372.

Shaver, G. R., J. A. Laundre, A. E. Giblin, and K. J. Nadelhoffer, 1996: Changes in live plant biomass, primary production, and species composition along a riverside toposequence in Arctic Alaska, U.S.A. *Arct. Alp. Res.,* **28,** 363–379.

Shreve, F., and I. L. Wiggins, 1964: *Vegetation and Flora of the Sonoran Desert*. Vol. 1. Stanford University Press, 178 pp.

Silverman, B. A., 1968: The effect of spatial averaging on spectrum estimation. *J. Appl. Meteor.,* **7,** 168–172.

Sims, D. A., H. Luo, S. J. Hastings, W. C. Oechel, A. F. Rahman, and J. A. Gamon, 2006: Parallel adjustments in vegetation greenness and ecosystem CO_2 exchange in response to drought in a Southern California chaparral ecosystem. *Remote Sens. Environ.,* **103,** 289–303.

Spiess, T., J. Bange, M. Buschmann, and P. Vörsmann, 2007: First application of the meteorological Mini-UAV 'M2AV.' *Meteor. Z.,* **16,** 159–169, doi:10.1127/0941-2948/2007/0195.

Sponseller, R. A., 2007: Precipitation pulses and soil CO_2 flux in a Sonoran Desert ecosystem. *Global Change Biol.,* **13,** 426–436.

Swinbank, W. C., 1951: The measurement of vertical transfer of heat and water vapor by eddies in the lower atmosphere. *J. Meteor.,* **8,** 135–145.

Telford, J. W., and P. B. Wagner, 1974: The measurement of horizontal air motion near clouds from aircraft. *J. Atmos. Sci.,* **31,** 2066–2080.

——, ——, and A. Vaziri, 1977: The measurement of air motion from aircraft. *J. Appl. Meteor.,* **16,** 156–166.

Thomas, R. M., K. Lehmann, H. Nguyen, D. L. Jackson, D. Wolfe, and V. Ramanathan, 2012: Measurement of turbulent water vapor fluxes using a lightweight unmanned aerial vehicle system. *Atmos. Meas. Tech.,* **5,** 243–257, doi:10.5194/amt-5-243-2012.

Tjernström, M., and C. A. Friehe, 1991: Analysis of a radome air-motion system on a twin-jet aircraft for boundary-layer research. *J. Atmos. Oceanic Technol.,* **8,** 19–40.

Tucker, C. J., 1979: Red and photographic infrared linear combinations for monitoring vegetation. *Remote Sens. Environ.,* **8,** 127–150.

Turner, D. P., S. V. Ollinger, and J. S. Kimball, 2004: Integrating remote sensing and ecosystem process models for landscape-to regional-scale analysis of the carbon cycle. *Bioscience,* **54,** 573–584, doi:10.1641/0006-3568(2004)054[0573:irsaep]2.0.co;2.

——, and Coauthors, 2005: Site-level evaluation of satellite-based global terrestrial gross primary production and net primary production monitoring. *Global Change Biol.,* **11,** 666–684.

Turner, R. M., and D. E. Brown, 1982: Sonoran desertscrub. *Biotic Communities of the American Southwest–United States and Mexico,* D. E. Brown, Ed., University of Arizona, 181–221.

Urban, J. R., L. Rojas-Bracho, H. Perez-Cortez, A. Gomez-Gallardo, S. Swartz, S. Ludwig, and R. L. Brownell Jr., 2003: A review of gray whales on their wintering grounds in Mexican waters. *J. Cetacean Res. Manage.,* **5,** 281–295.

Valiela, I., J. L. Bowen, and J. K. York, 2001: Mangrove forests: One of the world's threatened major tropical environments. *Bioscience,* **51,** 807–815, doi:10.1641/0006-3568(2001)051[0807:MFOOTW]2.0.CO;2.

van den Kroonenberg, A., T. Martin, M. Buschmann, J. Bange, and P. Vörsmann, 2008: Measuring the wind vector using the autonomous Mini Aerial Vehicle M2AV. *J. Atmos. Oceanic Technol.,* **25,** 1969–1982.

Vargas, R., H. W. Loescher, T. Arredondo, E. Huber-Sannwald, R. Lara-Lara, and E. A. Yépez, 2012: Opportunities for advancing carbon cycle science in Mexico: Toward a continental scale understanding. *Environ. Sci. Policy,* **21,** 84–93, doi:10.1016/j.envsci.2012.04.003.

Vellinga, O. S., B. Gioli, J. A. Elbers, A. A. M. Holtslag, P. Kabat, and R. W. A. Hutjes, 2010: Regional carbon dioxide and energy fluxes from airborne observations using flight-path segmentation based on landscape characteristics. *Biogeosciences,* **7,** 1307–1321, doi:10.5194/bg-7-1307-2010.

——, R. J. Dobosy, E. J. Dumas, B. Gioli, J. A. Elbers, and R. W. A. Hutjes, 2013: Calibration and quality assurance of flux observations from a small research aircraft. *J. Atmos. Oceanic Technol.,* **30,** 161–181.

Vermote, E. F., and N. Saleous, 2006: Operational atmospheric correction of MODIS visible to middle infrared land surface data in the case of an infinite Lambertian target. *Earth Science Satellite Remote Sensing: Science and Instruments,* J. J. Qu et al., Eds., Springer, 123–153.

——, and S. Kotchenova, 2008: Atmospheric correction for the monitoring of land surfaces. *J. Geophys. Res.,* **113,** D23S90, doi:10.1029/2007jd009662.

——, N. El Saleous, C. O. Justice, Y. J. Kaufman, J. L. Privette, L. Remer, J. C. Roger, and D. Tanré, 1997: Atmospheric correction of visible to middle-infrared EOS-MODIS data over land surfaces: Background, operational algorithm and validation. *J. Geophys. Res.,* **102** (D14), 17 131–17 141.

——, N. Z. El Saleous, and C. O. Justice, 2002: Atmospheric correction of MODIS data in the visible to middle infrared: First results. *Remote Sens. Environ.,* **83,** 97–111.

Vourlitis, G. L., J. Verfaillie, W. C. Oechel, A. Hope, D. Stow, and R. Engstrom, 2003: Spatial variation in regional CO_2 exchange for the Kuparuk River basin, Alaska over the summer growing season. *Global Change Biol.,* **9,** 930–941.

Walker, M. D., D. A. Walker, and N. A. Auerbach, 1994: Plant communities of a tussock tundra landscape in the Brooks Range foothills, Alaska. *J. Veg. Sci.,* **5,** 843–866.

Webb, E. K., G. I. Pearman, and R. Leuning, 1980: Correction of flux measurements for density effects due to heat and water-vapor transfer. *Quart. J. Roy. Meteor. Soc.,* **106,** 85–100.

Wiggins, I. L., 1980: *Flora of Baja California.* Stanford University Press, 1025 pp.

Williams, A., and D. Marcotte, 2000: Wind measurements on a maneuvering twin-engine turboprop aircraft accounting for flow distortion. *J. Atmos. Oceanic Technol.,* **17,** 795–810.

Williams, M., and Coauthors, 2009: Improving land surface models with FLUXNET data. *Biogeosciences,* **6,** 1341–1359, doi:10.5194/bg-6-1341-2009.

Wilson, K., and Coauthors, 2002: Energy balance closure at FLUXNET sites. *Agric. For. Meteor.,* **113,** 223–243.

Wohlfahrt, G., L. F. Fenstermaker, and J. A. Arnone, 2008: Large annual net ecosystem CO_2 uptake of a Mojave Desert ecosystem. *Global Change Biol.,* **14,** 1475–1487, doi:10.1111/j.1365-2486.2008.01593.x.

Wyngaard, J. C., 1988: The effects of probe-induced flow distortion on atmospheric-turbulence measurements: Extension to scalars. *J. Atmos. Sci.,* **45,** 3400–3412.

Zarate-Ovando, B., E. Palacios, H. Reyes-Bonilla, E. Amador, and G. Saad, 2006: Waterbirds of the lagoon complex Magdalena Bay-Almejas, Baja California Sur, Mexico. *Waterbirds,* **29,** 350–364.

Zhang, W. Q., W. Perrie, and S. Vagle, 2006: Impacts of winter storms on air-sea gas exchange. *Geophys. Res. Lett.,* **33,** L14803, doi:10.1029/2005GL025257.

Zulueta, R. C., W. C. Oechel, H. W. Loescher, W. T. Lawrence, and K. T. Paw U, 2011: Aircraft-derived regional scale CO_2 fluxes from vegetated drained thaw-lake basins and interstitial tundra on the Arctic coastal plain of Alaska. *Global Change Biol.,* **17,** 2781–2802, doi:10.1111/j.1365-2486.2011.02433.x.